https://doi.org/10.5194/egusphere-2026-2427
Preprint. Discussion started: 12 May 2026

Mineral dust concentration controlling convective cirrus structure and persistence: a large-eddy simulation study with observational constraints

Kasper Juurikkala[1], Tomi Raatikainen[1], Martina Krämer[2,†], Christina J. Williamson[1], and Ari Laaksonen[1,3]

[1]Finnish Meteorological Institute, 00560 Helsinki, Finland
[2]Institute for Physics of the Atmosphere (IPA), Johannes Gutenberg University, Mainz, Germany
[3]Department of Technical Physics, University of Eastern Finland, 70211 Kuopio, Finland
[†]formerly: Institute of Climate and Energy Systems (ICE-4), Research Center Jülich, Jülich, Germany

Correspondence: Kasper Juurikkala (kasper.juurikkala@fmi.fi)

Abstract. Dusty cirrus clouds are optically thick, convectively organized ice clouds that occur during intense mineral dust outbreaks. Previous modeling studies have found a link between mineral dust and convectively generated cirrus, but have been unable to explicitly resolve the associated convective dynamics due to limited spatial resolution. Here, we investigate the evolution and persistence of dusty cirrus using large-eddy simulations constrained by in-situ aircraft observations from the ML-CIRRUS 2014 campaign and complementary remote sensing data.

The simulations indicate that sustained convective cirrus requires mineral dust concentrations exceeding climatological values by approximately one to two orders of magnitude, corresponding to number concentrations on the order of $N_D \sim 1\ \mathrm{cm}^{-3}$. Under these conditions, heterogeneous freezing on mineral dust dominates ice formation and maintains sufficiently high ice crystal number concentrations to sustain strong longwave cooling at cloud top and preserve convective overturning under shortwave radiative warming. In contrast, homogeneous freezing remains largely suppressed across a wide range of simulated conditions. The direct radiative effect of mineral dust is comparatively weak relative to cloud radiative feedbacks and does not significantly influence cirrus evolution.

The simulated cirrus is also highly sensitive to the choice of deposition ice nucleation parameterization, highlighting a major source of uncertainty in representing dust–ice interactions. Overall, the results identify mineral dust availability as the primary control on dusty cirrus persistence and emphasize the need for improved representation of heterogeneous ice nucleation in atmospheric models.

1 Introduction

Dusty cirrus clouds, commonly observed in the vicinity of major dust sources worldwide, with common examples in strong Saharan (Kollath, 2010; Weger et al., 2018; Seifert et al., 2023) or East Asian dust (Zeng et al., 2023) outbreaks, present a unique and complex phenomenon. These cirrus clouds have a particularly defined convectional cell structures covering large areas. Nagy (2009) reported that the convective cell structures are almost exclusively associated with pres-

https://doi.org/10.5194/egusphere-2026-2427
Preprint. Discussion started: 12 May 2026

ence of dust high in the troposphere. These systems are associated with dust-infused baroclinic storms (DIBS; Fromm et al., 2016) that transport vast amounts of dust into the upper troposphere. Dusty cirrus clouds are typically associated with significant optical thickness and can substantially modify the radiative balance, especially over Europe and Central Asia, where these events are often observed. The dust influence has been reported to extend cirrus cloud lifetimes via heterogeneous freezing (Ansmann et al., 2019) even though heterogeneous freezing has usually been associated with decreased lifetimes of cirrus (e.g. Storelvmo et al., 2014; Gruber et al., 2019).

Current numerical weather prediction (NWP) models struggle to simulate dusty cirrus events accurately due to their limited ability to predict real-time mineral dust distributions and lacking cloud-aerosol interaction schemes. There are current efforts on building frameworks that would allow the dust-ice interaction to be implemented in NWP models such as European Centre for Medium-Range Weather Forecasts (ECMWF) Integrated Forecasting System (IFS) model. Seifert et al. (2023) proposed a dust-aware sub-grid parameterization scheme developed for ICOsahedral Nonhydrostatic model with Aerosol and Reactive Trace gases (ICON-ART) where they were able to simulate the formation of dusty cirrus for selected Saharan dust events and were thus able to substantially improve estimation of short- and longwave radiation fluxes that were observed with satellites. Regardless of the current understanding that the elevated dust levels is related to the presence of extensive cirrus layers, there is a need for more detailed investigations and improved parameterizations to enhance our understanding and predictive capabilities regarding these cloud systems.

In this study we use the UCLALES-SALSA (Calderón et al., 2025; Tonttila et al., 2017) model to simulate dusty cirrus clouds that were measured with in-situ instrumentation on the ML-CIRRUS 2014 campaign conducted with HALO aircraft on the April 4th. We focus on understanding governing factors controlling the evolution of dusty cirrus and exploring ways to improve large scale model representation of these systems. UCLALES-SALSA enables simulations of microphysical processes at high resolution, especially convection that even regional models with kilometer-scale resolution (Rieger et al., 2017; Weger et al., 2018; Seifert et al., 2023) are not able to directly simulate and thus is a perfect tool for simulations of convectively driven dusty cirrus clouds.

We conduct a series of sensitivity simulations varying the mineral dust number concentrations (N_D) from in-situ measured reference values to observe the conditions that allow the continuous extended lifetime of these dusty cirrus clouds. Additionally, the effects of radiative fluxes both of long wave (LW) and short wave (SW) radiation at the top of the cirrus clouds are explored in connection to the convective structures. We use remote sensing observations from cloud radar and satellite retrieval data to complement the in-situ observations.

2 Methods

2.1 UCLALES-SALSA

UCLALES-SALSA (v2.1) (Tonttila et al., 2017; Calderón et al., 2025) is a large-eddy simulation (LES) model combined with a sectional aerosol microphysics model SALSA (Sectional Aerosol module for Large-Scale Applications) (Kokkola

https://doi.org/10.5194/egusphere-2026-2427
Preprint. Discussion started: 12 May 2026

et al., 2008, 2018) extended for liquid and ice clouds (Tonttila et al., 2017; Ahola et al., 2020). UCLALES is a well known atmospheric LES model based on the work of Stevens et al. (1999, 2005). The aerosols and hydrometeors in SALSA are described with a sectional bin treatment, a computationally heavy but accurate approach to simulate the aerosol-cloud interactions. The computation of particle growth by condensation and deposition is based on theoretical descriptions without needing to rely on parametrized processes. SALSA has undergone several iterations after its implementation in the UCLALES model and now includes atmospheric processes from cloud droplet formation to ice nucleation and several secondary ice production processes (Calderón et al., 2025). Previously, the model has been used to explore ice nucleation processes in high altitude cirrus clouds (Juurikkala et al., 2025).

The aerosols and cloud droplets are described using a parallel dry-bins method, in which the particle number and mass are tracked on the basis of their dry size and internally mixed aerosol compositions. The aerosols are activated to cloud droplets when the wet size reaches the activation size via κ-Köhler method. The vapor condensation efficiency on aerosols is controlled by water activity on the basis of the soluble material content of aerosols, of which sulfate/organic/nitrate aerosols are soluble and dust/black carbon are insoluble. Primary ice nucleation mechanisms described within the model are homogeneous freezing, immersion freezing, and deposition ice nucleation (DIN). In this study, we use the approach of Koop et al. (2000) for homogeneous freezing of cloud and rain droplets (aqueous soluble aerosols) by stochastic nucleation process, which depends only on the activity of water in the droplets and the temperature. The DIN is described with deterministic schemes by Hiranuma et al. (2014) (hereafter H14), Ullrich et al. (2017) (hereafter U17), and Phillips et al. (2013) (hereafter P13). The deterministic heterogeneous freezing parameterizations (H14, U17 and P13) produce so called INAS (ice nucleation active site, n_s) densities (m^{-2}) that are temperature and relative humidity over ice (RHi) dependent. The frozen fraction of particles is then calculated for each particle size (D_p) using their corresponding surface area multiplied by INAS density as $FF = 1 - \exp(-n_s \pi D_p^2)$. Ice crystals are tracked in a single category bins spanning in range of $2\mu\mathrm{m} \leq D_i \leq 2$ mm. An important feature of deterministic ice nucleation parameterization schemes is that the frozen fraction needs to be tracked precisely. The SALSA microphysics is therefore modified by adding the advection of frozen fraction as well as the reverse calculation of frozen fractions when sublimation of ice crystals back to the aerosol phase takes place. To simplify the tracking of frozen fractions in the model domain, we omit the sedimentation and coagulation of aerosols.

In this study, we use the updated size dependent ice-phase microphysics adopted in Juurikkala et al. (2025) where ice diameters smaller than 40 µm are treated as spherical ice and for larger sizes as 5-sided bullet rosettes. These bullet rosettes are typically the dominant type in cirrus clouds of in-situ origin (Lawson et al., 2019). For this study, we implemented the ventilation effect for ice crystals as described in Sölch and Kärcher (2010) and updated the terminal velocity calculation as Mitchell and Heymsfield (2005) described. The deposition coefficient (α) is set to $\alpha = 0.2$ which, according to Lamb et al. (2023), provides the best description of ice crystal growth at temperatures above 210 K. The capacitance parameter is set to $C = 0.5$ for ice crystals smaller than 20 µm and to $C = 0.25$ for ice crystals greater than 50 µm. In the intermediate range $20 \leq D_i \leq 50\mu$m, C is set to the average between two size regimes to represent the presence of both spherical ice

https://doi.org/10.5194/egusphere-2026-2427
Preprint. Discussion started: 12 May 2026

crystals and bullet rosettes.

For dust-ice cloud-radiation interactions, Fu and Liou (1993) based radiation solver is used.

2.2 Observation data

2.2.1 In-situ measurement data of aerosols and ice

A HALO aircraft research flight was conducted on April 4 2014 as part of the ML-CIRRUS campaign (Voigt et al., 2017) targeting cirrus clouds over Western Europe. The HALO aircraft was equipped with multiple instruments that measured aerosols, ice properties, and meteorological conditions. This study uses aerosol measurements conducted with an optical particle counter (OPC GRIMM model 1.129). The OPC measures particles from 250 nm to 20 µm with the maximum size limited by the size of the aircraft inlet to 5 µm. The OPC measurements are used to derive the input dust size distributions (PSD) for SALSA with logarithmic fit functions. The ice crystal size distribution were measured using the combination of two instruments, NIXE-CAPS (CAS and CIP combined) (Meyer, 2012) and CCP. The CAS covers size ranges from 0.61 to 50 µm and thus measured both coarse size aerosols and smaller sizes of ice. On April 4th, the CIP instrument was not working and thus the CCP was used instead to measure size ranges from 50 to 945 µm. NIXE-CAPS measured both ice crystal number concentration (ICNC) and ice water content (IWC) based on the measured particle size distribution (PSD) which are used to evaluate the model ice nucleation. Sub-3 µm particles measure with CAS are considered aerosols, however, we do not use this aerosol information, but cover the entire relevant particle size range by using the OPC measurements. For the meteorological state parameters, the Basic HALO Measurement and Sensor System (BAHAMAS, Giez et al., 2021; Krautstrunk and Giez, 2012) measurements are used. For more detailed analysis of instrumentation performance and measurement results, please refer to Weger et al. (2018).

2.3 Remote sensing data

Cloud radar data were obtained with the METEK MIRA-35C Doppler cloud radar deployed at the Environmental Research Station Schneefernerhaus (UFS), Germany 47.417°N, 10.977°E; 2650 m a.m.s.l.) (location shown in Fig. 1b). The MIRA-35C is a high-sensitivity Ka-band (35 GHz) cloud radar. It employs a pulsed magnetron transmitter with a peak power of 30 kW and supports polarimetric measurements, enabling the derivation of parameters such as radar reflectivity, Doppler velocity and linear depolarization ratio (LDR). The post-processed radar data is provided from the Cloudnet data portal, a cloud remote sensing data repository within the Aerosol, Clouds and Trace Gases Research Infrastructure (ACTRIS). The dataset used in this study is described in Ewald et al. (2026). The Cloudnet processing framework applies a synergistic retrieval approach (Illingworth et al., 2007; Tukiainen et al., 2020), combining measurements from cloud radar, lidar, and microwave radiometer with thermodynamic profiles provided by the European Centre for Medium-Range Weather Forecasts (ECMWF) model. The key microphysical product used in this study is IWC which is retrieved in Cloudnet using the so-called Z–T method described by Hogan et al. (2006). The Z-T method relates the attenuation corrected

https://doi.org/10.5194/egusphere-2026-2427
Preprint. Discussion started: 12 May 2026

radar reflectivity factor to the model temperature through an empirical regression formula derived from in-situ aircraft measurements.

DARDAR (raDAR–liDAR) provides ice-cloud property estimates (such as ICNC and IWC) (Sourdeval et al., 2018), which combines measurements from the CloudSat 94 GHz Cloud Profiling Radar (CPR) and the CALIPSO Cloud-Aerosol Lidar with Orthogonal Polarization (CALIOP). The combined product of radar and lidar observations enables improved characterization of cirrus clouds compared to single-instrument retrievals.The combination of both instruments provides constraints to particle size distribution parameters (slope parameter N_0^* and volume-weighted diameter D_m) via a parameterization by Delanoë et al. (2005). From the estimated PSD, bulk microphysical properties are derived, including IWC and ICNC. The estimation of ICNC with DARDAR-ice algorithm provides ICNC for ice sizes above 5 μm. The vertical resolution of the DARDAR product is approximately 60 m, with a horizontal sampling of 1.6 km along the satellite track. In regions where the lidar signal is fully attenuated, the retrieval relies predominantly on radar information, which can increase uncertainty, particularly for low IWC conditions typical of cold upper-tropospheric cirrus. Published uncertainty estimates for IWC are typically on the order of 30–60%, depending on cloud optical depth and microphysical regime. In this study, DARDAR vertical profiles of IWC and ICNC are used to characterize the observed dusty cirrus structure and to provide an independent constraint for evaluating the modeled microphysical properties.

For the large scale analysis of cloud top temperatures, we utilize SEVIRI MSG (EUMETSAT) retrieval data for cloud brightness temperatures at 8.7μm wavelength since it serves a good proxy for cloud top temperature for optically dense cirrus. The brightness temperatures in the analysis are restricted to values below 230 K which represent the dusty cirrus temperature regime.

2.4 Dusty cirrus of 02–05 April 2014

On April 2nd 2014, a cut-off low-pressure system developed over the Iberian Peninsula and propagated eastward while intensifying. Along the eastern flank of the system, a developing and strengthening warm conveyor belt (WCB) leading a cold front produced high surface winds and resulted in high emissions of mineral dust over northern Sahara around Atlas Mountains and Moroccan-Algeria border that were transported by WCB to higher in troposphere (Weger et al., 2018). MSG Seviri IR satellite imagery (not shown) on April 3rd reveal an extensive region of dusty cirrus associated with convective cells embedded within the WCB outflow and by April 4th the dust was transported over a large area over Europe which was identifiable as large shield of cirrus. As part of the ML-CIRRUS campaign, research flights using HALO were conducted to sample these clouds. On April 4th, the aircraft intercepted and directly measured the extensive cirrus layer as shown in Fig. 1 a, b.

Figure 2 shows the vertical profile of measured concentrations of aerosols and ice below 9.5 km where the OPC measured elevated concentrations of aerosols for total number and filtered for sizes above 500 nm above 7 km, showing that the Saharan dust plume had still quite high concentrations of large dust particles. Roughly at 8 km, HALO encountered near supersaturated conditions over ice with high ICNC values that were most likely connected to the elevated presence of dust

https://doi.org/10.5194/egusphere-2026-2427
Preprint. Discussion started: 12 May 2026

Weger et al. (2018).

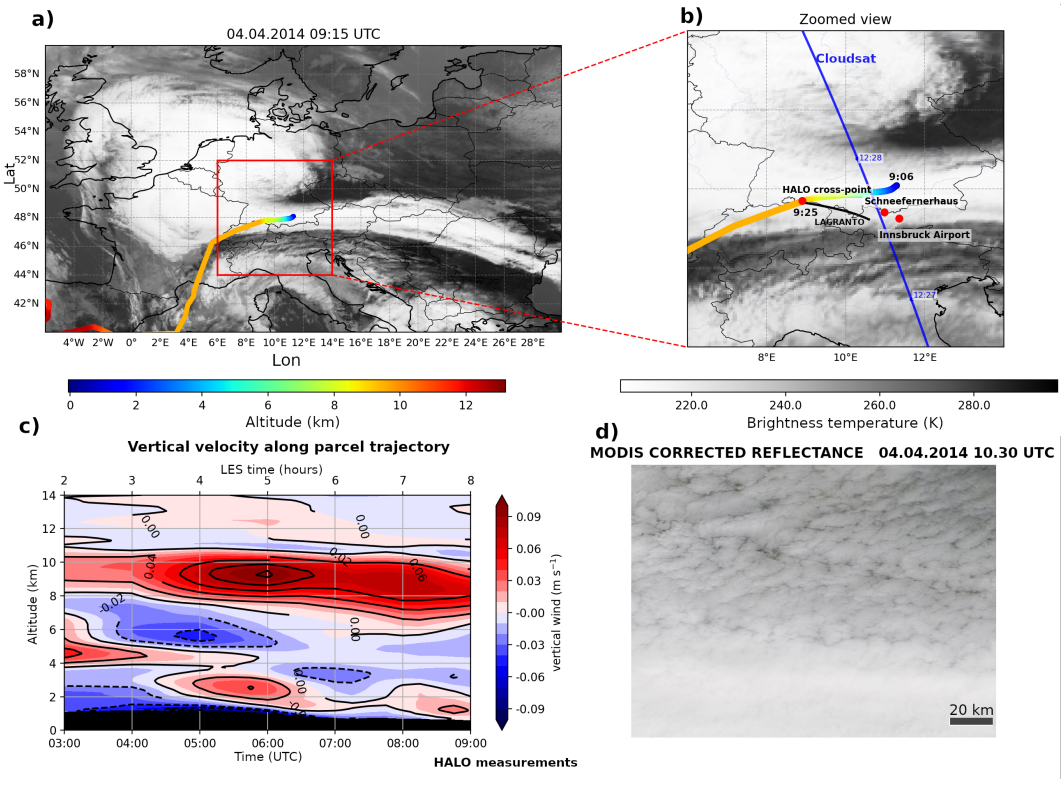

Figure 1. MSG IR 8.7 µm channel imagery over Europe a) with zoomed view with LAGRANTO 6 hour parcel trajectory (black solid line) and observation points marked with red dot b). Panel c) shows the vertical velocity forcing term from ERA5 along the parcel trajectory shown in b). Panel d) shows more detailed view of cirrus observed by Moderate Resolution Imaging Spectroradiometer (MODIS, NASA) at visible spectrum.

Sounding profile measured at Innsbruck Airport (Austria) at 03:00 UTC on 4 April (Fig. 4a black solid line) suggests that a layer with a small vertical gradient in potential temperature ($\partial\theta/\partial z$), indication of potential instability, was located below the tropopause layer at 9–11 km, supporting the idea that convective cirrus structures are the result of instability. Vertical gradient of equivalent potential temperature (Eq. A1) shows whether phase change within the cirrus leads to new development of convective cells under large scale lifting as shown in Fig. 1. In the sounding profile between 9–11 km, we find potentially unstable layer with negative vertical gradients in equivalent potential temperature ($\partial\theta_e/\partial z < 0$), indication of convective generation. Additionally, the horizontal wind velocity profile suggest weak shear within the unstable layer with $\frac{du}{dz} \approx 2 \times 10^{-3}$ s^{-1} and the Richardson Number at $Ri \gg 0.25$, comfortably over the threshold where shear would cause vertical motions over buoyant forces.

The sounding evidence for an unstable layer between 9 and 11 km is supported by the presence of organized up- and

https://doi.org/10.5194/egusphere-2026-2427
Preprint. Discussion started: 12 May 2026

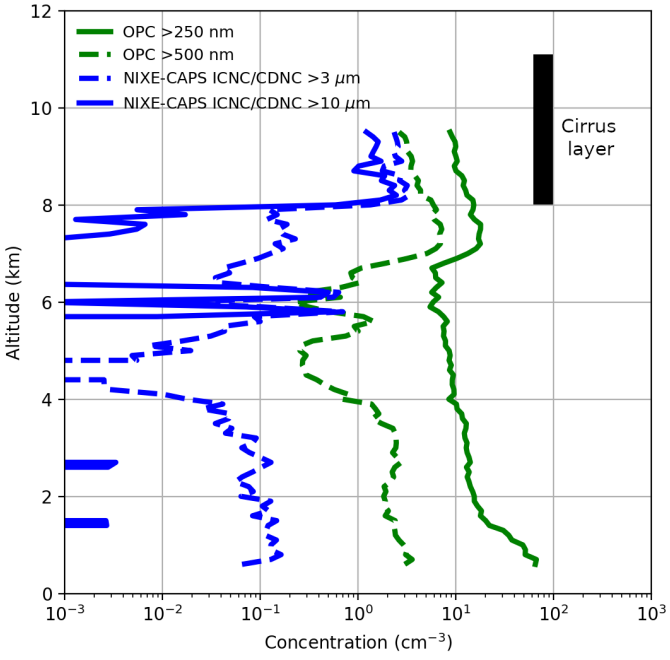

Figure 2. Vertical profile of NIXE-CAPS and OPC measured concentrations of ice and aerosols respectively during the HALO vertical ascent up to 9.5 km between 9.22-9.25 UTC. Extent of cirrus layer is marked with black vertical line between 8-11 km.

165 downdrafts in the MIRA-35C Doppler velocity observations at Schneefernerhaus (approx. 50 km from Innsbruck) during the early hours of April 4 (Fig. 3). We define the convective layer as CONV as shown in Fig 3 panels a and b.

The layer between 8–9 km (Fig. 4a) is moderately stable and cirrus forming at this level is forming from the influence of large-scale dynamics or from ice crystals sedimenting from the CONV. For this reason we refer to this layer as SEDI 170 as shown in Fig 3 panels a and b.

2.5 UCLALES-SALSA simulations of the dusty cirrus event

To investigate the microphysical mechanisms controlling the observed dusty cirrus clouds, we performed UCLALES-SALSA simulations designed to represent the evolution of the air mass sampled by the HALO aircraft at 9 UTC on April 175 4th (in Fig. 1b). The model domain is designed to follow a 6 hour kinematic trajectory using Lagrangian Trajectory Tool (LAGRANTO; Sprenger and Wernli, 2015). This trajectory was set to arrive at the HALO sampling point at 47.7°N,8.9°E at 200-hPa altitude and the origin point in the near proximity of the sounding conducted at Innsbruck Airport (Austria) at

https://doi.org/10.5194/egusphere-2026-2427
Preprint. Discussion started: 12 May 2026

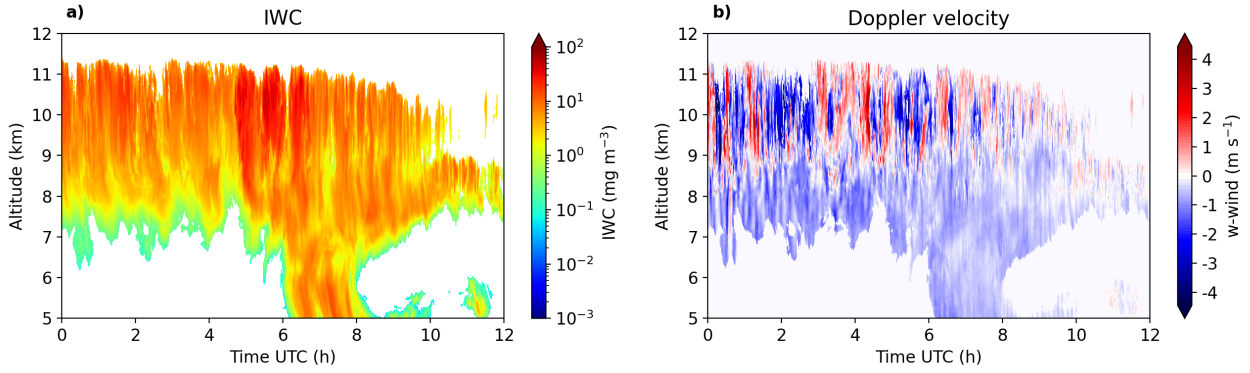

Figure 3. Time-altitude profile of IWC a) and Doppler wind (vertical) b) observed with MIRA-35C at Schneefernerhaus site on 04.04.2014.

3 UTC. We use a three-dimensional model domain with horizontal extension of $L_x = L_y = 24$ km with horizontal resolution $\Delta x = \Delta y = 150$ m. Vertical domain extension is set in the range of $0 \leq z \leq 14$ km with vertical resolution of $\Delta z =$ 50 m. Above 12 km, the resolution is increased to $\Delta z = 300$ m by 14 km. The simulation time is set with 2 hour spin up period followed by 6 hour simulation which represents the cloud evolution along the LAGRANTO parcel trajectory. Output is written with 5 min interval. Additionally, the model domain follows solar diurnal cycle at latitude 47.5° and therefore experiences both nighttime conditions in the initial 2.5 hours and daytime conditions for the latter half of the simulation time.

The sounding profile is used as a reference for model domain input meteorology albeit with small modifications allowing proper initialization of convection. The humidity profile is modified to quickly initialize cirrus convection with a high relative humidity over ice (RHi) set between 8.5 and 10.8 km (as shown in Fig. 4). The solid red RHi profile line in Fig. 4 is close to the Koop et al. (2000) threshold line for homogeneous freezing but does not cross it as we do not want to cause immediate burst of homogeneous freezing at the initial time step when the ice nucleation process is triggered. The integrated RHi profile corresponds to mean total vapor content (measured with BAHAMAS combined with NIXE-CAPS IWC) inside the dusty cirrus. Additionally, the model input potential profile between 8.8–11 km is set at fixed gradient of $\partial\theta/\partial z = 0.1$ K km^{-1} which corresponds to the lowest stability simulations by Fusina and Spichtinger (2010) and the mean gradient in the sounding profile. The input potential temperature profile is slightly different than the sounding profile as we need to consider temperature profile change during the spin up period when intense latent heat release associated with vapor-ice phase transfer occurs. Also, we do not use the potential temperature gradient of the sounding between 8.8–11 km since the measured profile has varying temperature gradient influenced by active convection. Additionally, the measured sounding shows very high similarity in temperatures measured by BAHAMAS six hours later in time and in

https://doi.org/10.5194/egusphere-2026-2427
Preprint. Discussion started: 12 May 2026

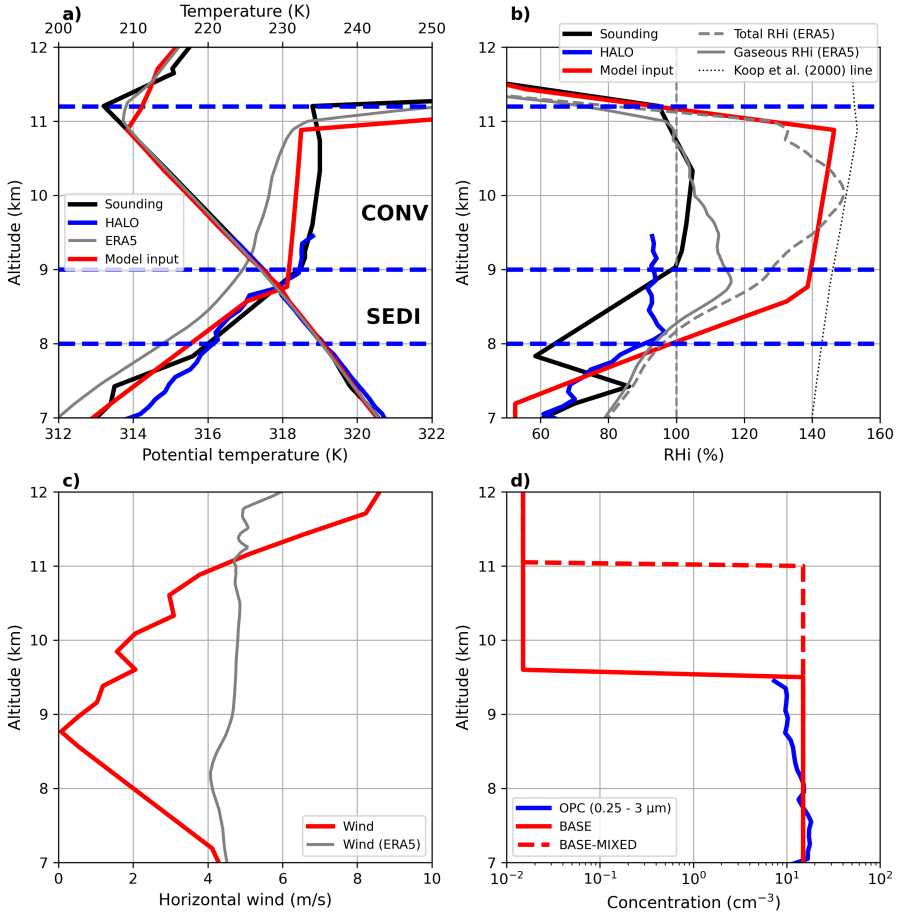

Figure 4. Model domain initial profile (red solid) for cirrus runs based on sounding (black solid) from Innsbruck, Austria starting at 03 UTC on 04.04.2014. BAHAMAS measured temperatures are shown on top of the sounding line (blue solid). The aerosol concentration (blue solid) is from OPC for particle sizes above 250 nm. Dashed line for aerosol concentration shows the model run using pre-mixed dusty cirrus layer. ERA5 values are shown with thin grey lines at the initial point in the 6-hour LAGRANTO parcel trajectory. Convective layer (CONV) and sedimentation layer (SEDI) are marked with dashed blue lines.

spatially different locations, meaning that co-location via parcel trajectories is justified.

200

During the 6 hour simulation following the LAGRANTO parcel trajectory, we apply large scale vertical velocity forcing term on to the model domain with the temporal evolution shown in Fig. 1c occurring between 3–9 UTC based on vertical

https://doi.org/10.5194/egusphere-2026-2427
Preprint. Discussion started: 12 May 2026

wind from ERA5 (no forcing during spin up). We can see that the vertical velocity is initially weaker with $w_{\mathrm{LS}} = 3\ \mathrm{cms}^{-1}$ with the strongest forcing around 9–10 km in altitude. The w_{LS} is stronger between 5–9 UTC with maxima at $w_{\mathrm{LS}} = 10$ cms^{-1}. The dusty cirrus thus had experienced a strong synoptic forcing right before the aircraft observed these clouds around 09 UTC and this is visible as higher RHi values below 9 km in altitude compared to sounding RHi 6 hours prior (Fig. 4). Satellite imagery (Fig. 1) shows that the cirrus was optically thicker around the location of the aircraft observations and that the optically thick cirrus extended in the West-East direction with very similar cloud top temperatures, indicating that the cloud top altitude was at similar levels over large area and convection occurred under similar conditions. On top of large scale vertical velocity forcing, we nudge the horizontal winds towards ERA5 winds with relaxation time of 3 hours. This set up roughly follows the semi-Lagrangian style set up as used in Kazil et al. (2021), however, we omit here the influence of horizontal advection and nudging of temperature and humidity profiles since the initial state from sounding and final state from BAHAMAS observations are very similar in both temperature and humidity. Changes in RHi during six hours indicate that ambient conditions are mostly controlled by vertical velocity forcing, simplifying our setup.

Due to the lack of in-situ measurements above 9.5 km altitude inside the cloud layer (as shown in Fig. 2), we do not know

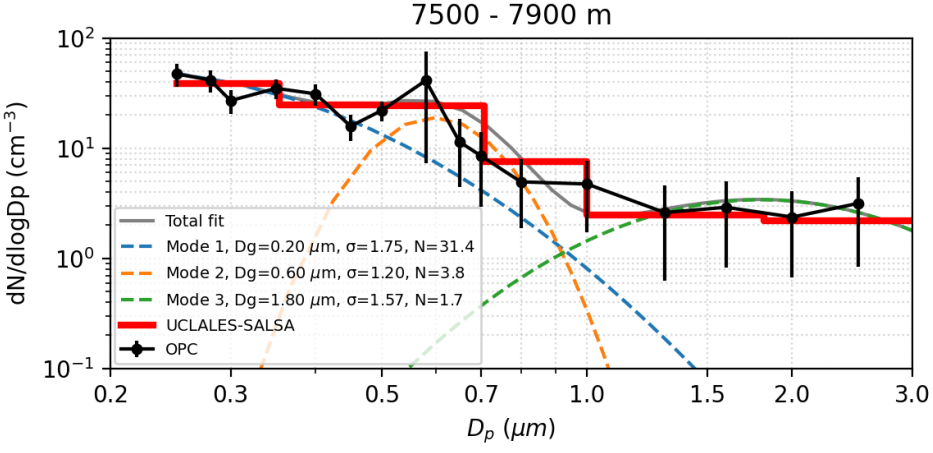

Figure 5. OPC measured aerosol size distribution right below the dusty cirrus cloud layer between 7.5 and 7.9 km altitudes shown with black dots with connecting solid lines and vertical standard deviation error bars. Fitting was done to the data to produce three modes for SALSA input and is shown with solid grey line. Modes contributing to the total fit is represented with dashed colored lines. Red solid line indicates the UCLALES-SALSA dust size distribution based on the lognormal modes.

the dust concentrations up to the cirrus top, however, we can estimate based on the in-situ vertical concentration profile in Fig. 2 and the assessment made by Weger et al. (2018) that dust was effectively mixed inside the convective layer and can be assumed to be roughly constant thorough the cirrus.

To construct the input dust profile for SALSA, we used OPC-derived PSD measurements obtained between 7.5 and 8 km

https://doi.org/10.5194/egusphere-2026-2427
Preprint. Discussion started: 12 May 2026

altitude at aerosol concentration $N_D = 15\ \mathrm{cm}^{-3}$ for particles in size range $0.25 \leq D \leq 6\ \mu$m, corresponding to clear-air conditions directly below the dusty cirrus layer. The measured PSD was fitted with three lognormal modes, which were then inputted into the insoluble aerosol bins in SALSA (Fig. 5). The aerosols measured by OPC are considered to consist of mineral dust particles that are all potential INPs. As the SALSA dust bins extend up to 6 µm, we extrapolate the dust PSD based on the Mode 3 shown in Fig. 5. NIXE-CAPS measurements above 3 µm confirm the continuation of the aerosol PSD which makes this extrapolation justified.

Two vertical configurations were considered to address uncertainty in the dust distribution above the observed layer. In the BASE configuration, constant mineral dust number concentration (N_D) was applied between 6 and 9.5 km. In the BASE-MIXED configuration, the same concentration was extended up to 11 km. These two cases cover the plausible range of dust vertical extent, given the lack of direct measurements above 9.5 km.

The BASE-MIXED setup is further motivated by the mixing hypothesis proposed by Seifert et al. (2023), which suggests that mineral dust can become vertically homogenized throughout the cirrus layer during its evolution.

For smaller than 0.25 µm, particles are treated as soluble sulfate type particles with $N_a = 300\ \mathrm{cm}^{-3}$, with lognormal distribution with geometric mean diameter of $\mu_D = 50$ nm and standard deviation $\sigma = 1.4$. The parameters are based on the configuration presented in Spichtinger (2014) with typical value for upper troposphere Minikin et al. (2003). These particles can participate in homogeneous freezing.

To study the effects of N_D on the evolution of dusty cirrus clouds, we vary the N_D from 0.01 to 10 cm^{-3} with a magnitude increment added with the mixed state dust profile, totaling five simulations ($N_D \approx 10\ \mathrm{cm}^{-3}$ corresponds to the BASE). The BASE and sensitivity runs are simulated using H14 as the main DIN parameterization scheme. Additionally, we make simulations using the BASE configuration and two complimentary parameterizations, U17 and P13 schemes, to investigate the sensitivity of the results to the choice of ice nucleation parameterization.

SALSA output for the ice bins is given in terms of spherical-equivalent diameter, whereas NIXE-CAPS provides the maximum dimension of ice crystals. To improve comparability with observations in the results section, the SALSA ice bins are converted to maximum dimension using the cirrus parameterization of Schumann et al. (2011).

3 Results and discussion

3.1 BASE simulation and comparison with observations

In this section, we present results from the BASE simulations and compare the model results against observations. All primary analyses are conducted using H14. U17 and P13 are used to assess sensitivity of ice nucleation pathways and to quantify structural uncertainty in simulated ICNC, IWC, and radiative feedbacks and are discussed separately in Sect. 3.1.2.

Figure 6 shows the temporal evolution of the dusty cirrus in the model domain for BASE simulation, mimicking a vertically scanning pointing cloud radar as in Fig. 3. The simulated cirrus exhibits enhanced IWC near cloud top and a vertical

https://doi.org/10.5194/egusphere-2026-2427
Preprint. Discussion started: 12 May 2026

structure consistent with the radar observations. Elevated vertical velocities occur primarily between 9 and 11 km, corresponding to the CONV layer below the tropopause shown in Fig. 6.

As shown in Fig. 6, updraft and downdraft regions are closely co-located with enhanced and reduced IWC, respectively,

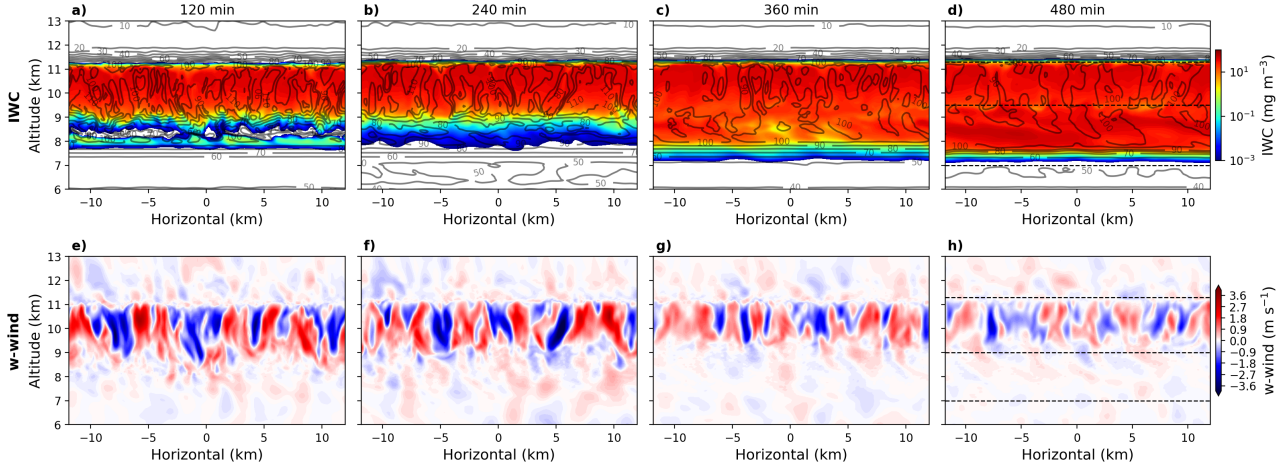

Figure 6. UCLALES-SALSA simulated IWC (upper panels, a-d) and vertical velocity component of wind (lower panels, e-h) at 2 hours time intervals (columns) during the BASE run. At last time step (480 min), CONV and SEDI layer altitude thresholds are marked with dashed lines.

indicating organized convective overturning. Rising convective cells originate near the cloud base, where new ice nucleation and recycled ice crystals increases IWC through depositional growth. The associated latent heat release warms the ascending parcels relative to their environment, reinforcing the updraft. As the air rises and cools moist adiabatically, RHi increases, promoting further ice nucleation and vapor deposition. Upon reaching the tropopause inversion, vertical flows are redirected horizontally. Local convergent flow between adjacent cells induces compensating subsidence, leading to adiabatic warming and subsaturation over ice, and thus reduced IWC. Downdraft regions are also microphysically important. Sublimation releases mineral dust particles that previously nucleated ice, allowing them to participate again in ice formation when re-entrained into updrafts.

Analysis of the temperature tendencies (according to Eq. A2) within the CONV layer shows that the convection was sustained by strong LW cooling at the cloud top as shown in Fig. 7, while LW heating was concentrated in the lower part of the dusty cirrus layer (Ovchinnikov et al., 2014). This mechanism was hypothesized as the main supportive mechanism for convection in dusty cirrus clouds in Weger et al. (2018) and Seifert et al. (2023). Towards the end of the simulation, SW radiation interrupts the LW cooling effect increasingly as the solar angle increases, the SW radiation flux increases, however, not enough to result in neutral heating. While the SW radiation did not disrupt the convection to the point of convection collapse, clear slowdown of convection as shown in Fig. 7 occurred as lower heating rates coming from turbulent mixing decreased substantially within the dusty cirrus. Also, in the latter half of the simulation, as the dusty cirrus layer widened under the influence of w_{LS} forcing, the LW warming spread out over wider layer and suppressed net heating rate

https://doi.org/10.5194/egusphere-2026-2427
Preprint. Discussion started: 12 May 2026

within the whole CONV layer as shown in the Fig. 7. The impact of radiation on dusty cirrus evolution is more closely discussed in Sect. 3.2.2.

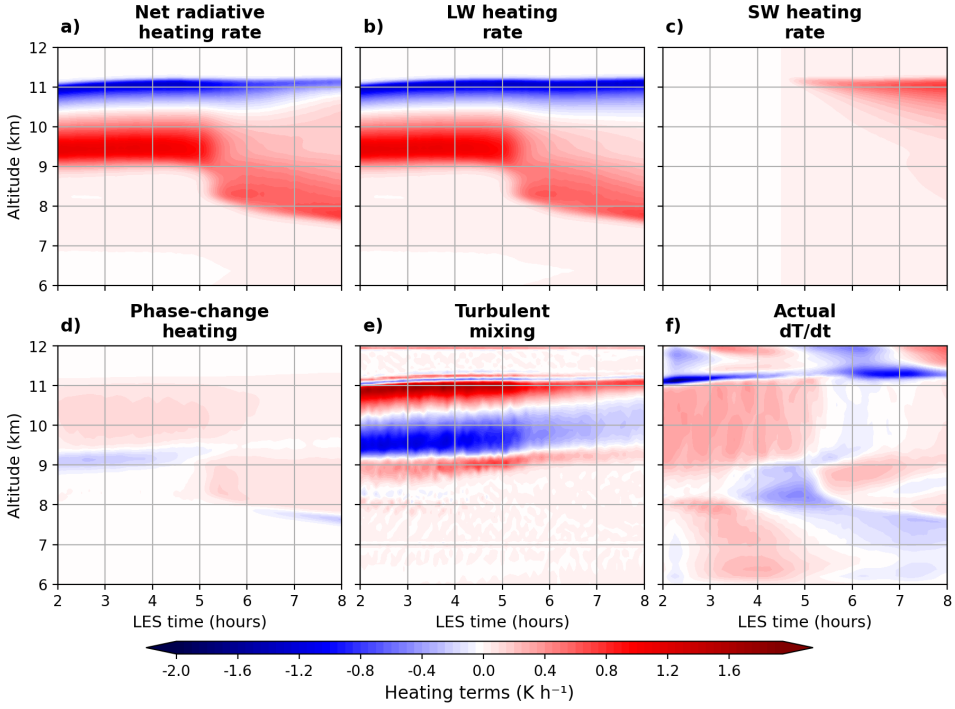

Figure 7. Heating rates for each term presented in Eq. A2 excluding the large-scale forcing in the BASE run (a-f).

In both MIRA-35C Doppler velocity observations (particle velocity not directly equivalent to true wind velocity) and model vertical wind (w), the variability of w increases with altitude as shown in Fig. 8. At 10.5 km level, in the middle vertically of the CONV layer where the w variability was also highest in the BASE run, the magnitude and distribution of w are in particularly close agreement, indicating that the model captures the essential dynamical character of the convective overturning. The simulated peak vertical velocities reach up to 2.5 ms^{-1}, similar magnitudes as what MIRA-35C observed at this level. The skewnesses of the distribution shape is also a telltale sign of convection as the peak frequency is found around 0.5 ms^{-1}.

Also at 9.5 km level, model, MIRA-35C, and BAHAMAS measurements produce a very similar shape of the distribution. The negative skewness of the velocity distributions at 9.5 km further indicate that this level is influenced by the descending branch of the convective circulation rather than active updraft cores. The overall agreement in dynamical structure provides confidence that the model is physically credible and that the coupling between dynamics and microphysics is realistically represented.

https://doi.org/10.5194/egusphere-2026-2427
Preprint. Discussion started: 12 May 2026

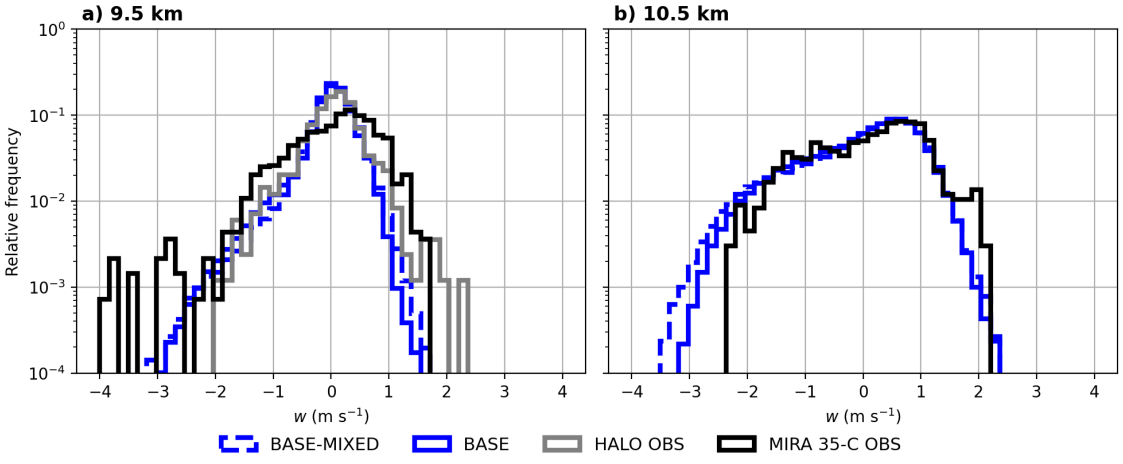

Figure 8. Model vertical wind compared with in-situ measurements at 9.5 km and MIRA-35C Doppler velocities at 9.5 and 10.5 km.

We must note that MIRA-35C observations in the Fig. 8 represent w measured between 6-8 UTC and not exactly at 9 UTC since the dusty cirrus layer had moved away from the Schneefernerhaus station by that time. However, because the observed w profiles varied only little during the whole observed time period covered by dusty cirrus layer, w profiles

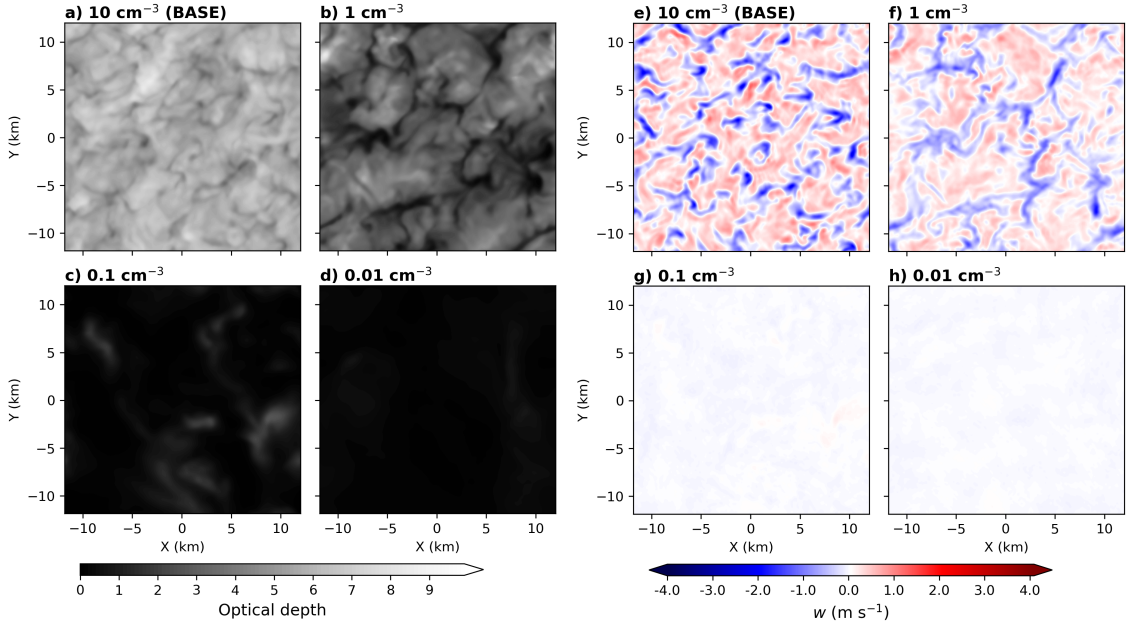

Figure 9. Optical depth for cirrus for varied N_D (a-d). Vertical wind is calculated as mean wind within the CONV layer between 9–11.5 km (e-h).

https://doi.org/10.5194/egusphere-2026-2427
Preprint. Discussion started: 12 May 2026

can be safely compared against the model and BAHAMAS measurements. We believe that at 9.5 km, MIRA-35C had observed slightly higher w variability since as it was shown in Fig. 6, the base of the CONV layer lifted towards the end of the run, coinciding with the reduced w variance in the model at 9.5 km.

Additionally, Fig. 9a,e shows the BASE domain cellular structure of the dusty cirrus clouds viewed from satellite perspective. Compared with MODIS (On board TERRA, NASA) visible imagery in Fig. 1d, almost identical structures were present over the model target area and larger area in the vicinity, suggesting that the simulated dusty cirrus could be used as generalized representation for dusty cirrus that occurred on April 4th.

3.1.1 Comparison of microphysical properties

We compare here the model performance at the end of the BASE and BASE-MIXED simulations which corresponds to the time when HALO measured dusty cirrus layer. The modeled IWC vertical profile generally agrees well with the range of in-situ measurements (differences between BASE and BASE-MIXED are very small) and with DARDAR-ice profiles obtained during the noon overpass as shown in Figure 10a. Agreement is less strong with MIRA-35C estimated IWC values, which are lower than both NIXE-CAPS and DARDAR observations. The common feature in modeled and observed cirrus is the shape of the IWC profile between 9 and 11.5 km (CONV) where the IWC increases towards the cloud top. While IWC was not sampled above 9.5 km with NIXE-CAPS, the IWC agrees well in the sampled altitude range.

For ICNC, the vertical profile has a very similar shape to the IWCs in the CONV (Fig. 10b) for both BASE and BASE-MIXED cases. The modeled ICNC varies in the model domain over a magnitude throughout the layer while with the NIXE-CAPS measurements, the variability is smaller. We must note that the NIXE-CAPS measurements of ICNC in the range of 8–9.5 km (SEDI) was a result of a single ascent sampling through cirrus which means that the variability is naturally small. For 9.5 km level, where HALO flew at constant altitude, the ICNC variability is significantly higher similarly to the model values. Regardless, the model ICNC is around an order of magnitude lower than NIXE-CAPS at SEDI layer, indicating that the model could underestimate ice production in temperature range $225 \leq T \leq 235$ K here. DARDAR-ice estimates of ICNC ($D_i > 5$ µm) on the other hand have a very similar vertical profile with slightly lower means and variability than the model means with BASE and BASE-MIXED runs. To ensure the model and NIXE-CAPS data comparability with DARDAR-ice, we calculated ICNC for over 5 µm ice for NIXE-CAPS and model and found only marginal changes to ICNC, suggesting that DARDAR-ice estimates should be roughly same for total ICNC. Additionally, although we do not have full coverage of dust measurements up to the dusty cirrus top, the model results indicate that dust mixes very efficiently throughout the dusty cirrus layer and the OPC measurements agree with the trend visible above 8 km in the model, where the concentration of dust decreases as shown in the Fig. 10c. The BASE simulation shows highest similarity to OPC measurements, while BASE-MIXED is still within the variability but in the upper range of measurements.

https://doi.org/10.5194/egusphere-2026-2427
Preprint. Discussion started: 12 May 2026

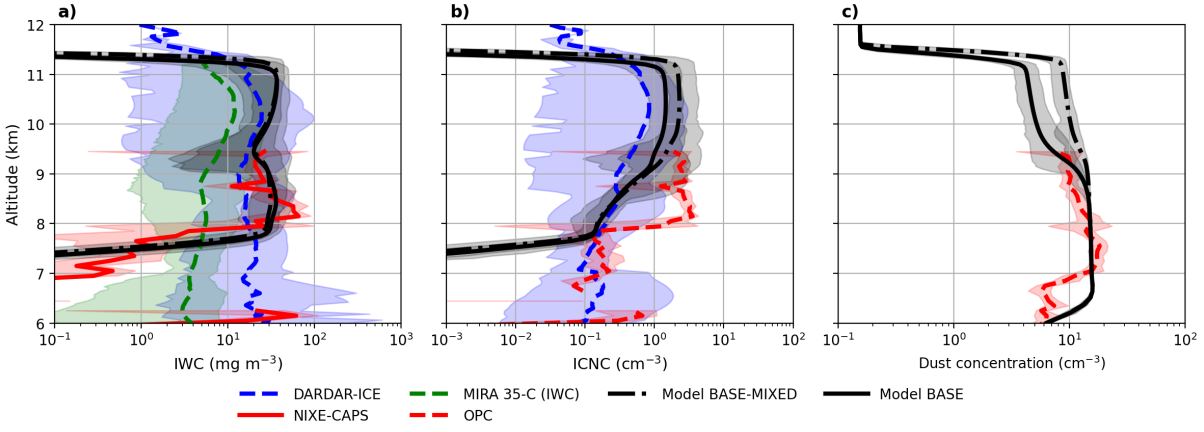

Figure 10. Model ICNC with UCLALES-SALSA (black solid line) versus DARDAR retrieval (blue dashed), cloud radar MIRA-35C at Schneefernerhaus (green dashed), and in-situ measurements (red dashed) of IWC a), ICNC with NIXE-CAPS b) and dust number concentration from OPC c). UCLALES-SALSA results are shown for the final time step closest in thermodynamic state to the CloudSat overpass at 11.50 UTC. MIRA-35C IWC is based on observations between 6 and 8 UTC, closest temporally to NIXE-CAPS and OPC measurements. Shading shows the full variability of measured and simulated values.

We compare the ice PSD (ISD) at 9.5 km level for BASE and BASE-MIXED simulations in Fig. 11a, where the ice crystals observed with NIXE-CAPS were most likely formed in the convectively driven cirrus (CONV layer). At this level, the modeled ISD agrees closely with NIXE-CAPS observations in both shape and magnitude showing that the model captures well the ice crystal growth. However, inside the SEDI layer (below 9 km), concentration of ice sizes below $D < 40\mu$m are underestimated as DIN was not particularly active at the final model time step due to strong suppression of RHi influenced by high IWC.

The large number of ice below 30 µm, in both observations and model, indicates that the measured ice was most likely very recently formed. We think that the measurement variability in ISD for smaller sized ice comes partially from the influence of background aerosol PSD overlapping with the ISD, since the NIXE-CAPS cannot distinguish between ice and aerosol particles. NIXE-CAPS (bins above 3 µm) measurements below the cirrus layer showed that aerosol concentrations were relatively high even at 10 µm. For the Fig. 11, we thus subtracted the background aerosol size distribution measured with NIXE-CAPS within the ice category bins which resulted in measured ISD to agree better with the modeled ISD.

3.1.2 Choice of DIN scheme and sources of ICNC uncertainty

DIN is the primary driver of ICNC in the simulated dusty cirrus. To assess the sensitivity to the choice of parameterization, simulations using H14, U17, and P13 are compared (Fig. 12). While the overall dynamical structure of the cirrus remains similar across simulations, substantial differences arise in ICNC and its vertical distribution.

https://doi.org/10.5194/egusphere-2026-2427
Preprint. Discussion started: 12 May 2026

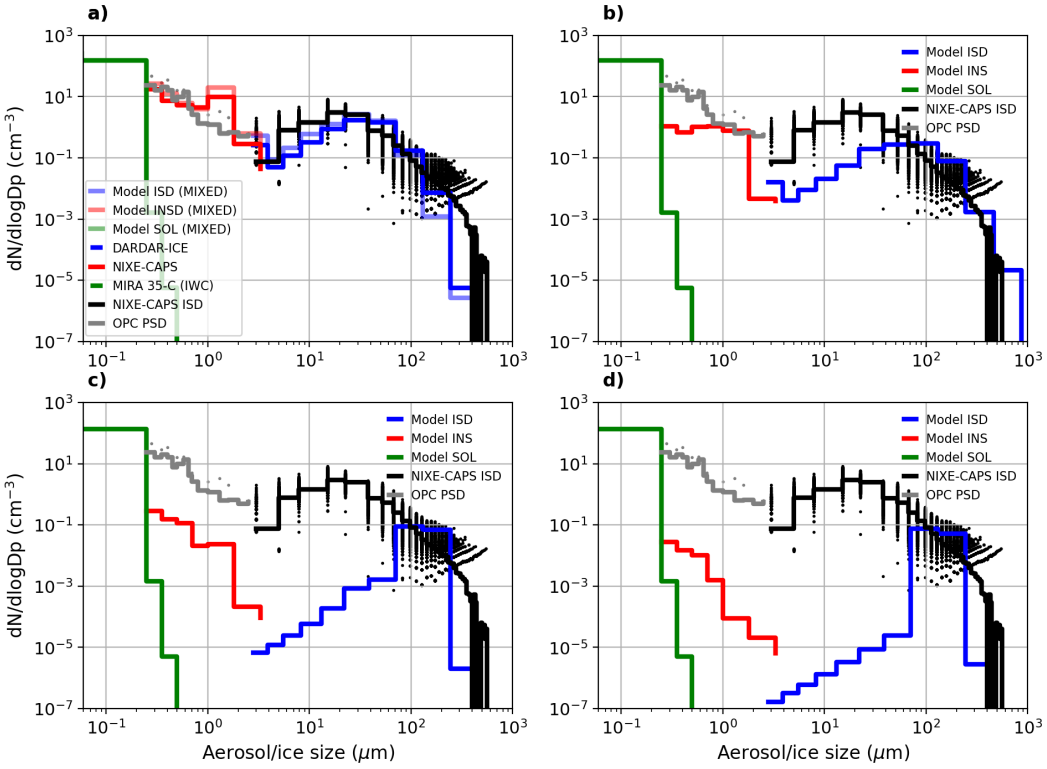

Figure 11. Particle size distributions of SALSA output for varied N_D (10, 1, 0.1 and 0.01 cm^{-3}) a-d and HALO observations. Model level for 9.5 km was used to compare with measurements at constant altitude leg at 9.5 km inside the cirrus with corresponding temperature T=223 K. The a-panel represents the BASE and BASE-MIXED simulation PSDs. INS stands for insoluble PSD and SOL for soluble PSD

These differences originate from the distinct temperature and RHi dependencies of the parameterizations at temperatures below 210 K (as shown in Fig. B1). The H14 scheme assumes a relatively low RHi threshold and weak temperature dependence between $210 \leq T \leq 220$ K, corresponding to temperatures at CONV, thus resulting in vertically more homogeneous ICNC profiles. In contrast, U17 produces increasing nucleation efficiency toward colder temperatures, producing maximum ICNC near cloud top with positive vertical gradient throughout the CONV layer. The P13 scheme on the other hand produces the lowest ICNC among all simulations, with ICNC only exceeding 10^{-2} cm^{-3} but with substantially weaker nucleation activity. The P13 IWC profile shows a clear lack of high IWC cloud top feature present in H14 and U17 cases. This behavior is consistent with previous findings in Weger et al. (2018), where they reported underestimation of cirrus evolution using the Phillips et al. (2008) formulation updated in Phillips et al. (2013).

The earlier onset of ice nucleation in H14, due to higher DIN activity at warmer temperatures, promotes depositional growth under conditions of higher water vapor availability (e.g., Murphy and Koop, 2005), leading to enhanced IWC compared to U17. This contributes to stronger latent heating within the convective layer and supports the maintenance of

https://doi.org/10.5194/egusphere-2026-2427
Preprint. Discussion started: 12 May 2026

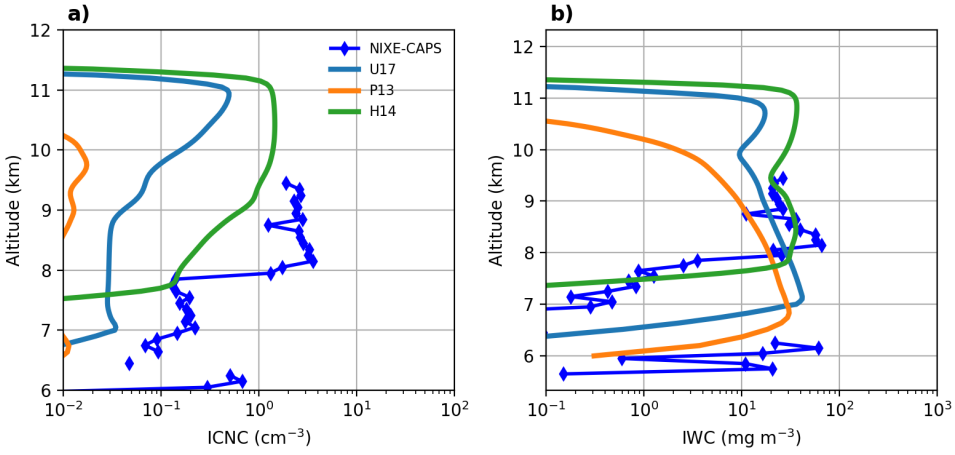

Figure 12. Model results using complimentary parameterization schemes for DIN (U17, P13, H14) versus NIXE-CAPS measured ICNC a) and IWC b).

its vertical extent. These results demonstrate that the choice of DIN parameterization exerts a major control on ice formation, cloud structure, and associated radiative feedbacks. Among the tested schemes, H14 provides the closest agreement with observations and is therefore used as the baseline parameterization in this study.

Despite simulations using different parameterization scheme, a systematic underestimation of ICNC remains at lower parts of the dusty cirrus compared to measurements, indicating limitations in current ice nucleation parameterizations. Laboratory studies have shown that certain mineral dust types, such as clay minerals, can nucleate ice efficiently at RHi values close to ice saturation (Möhler et al., 2006; Koehler et al., 2010; Welti et al., 2009, 2014), with weaker temperature dependence than represented in H14. Furthermore, the use of INAS density formulations may underestimate nucleation efficiency for smaller particles, particularly below 230 K where particle size dependence has been found to be weak (Welti et al., 2009). None of the parameterizations used here fully capture this high nucleation efficiency, which likely contributes to the ICNC underestimation.

On the other hand, homogeneous freezing does not compensate for this deficit under the simulated conditions. At the temperatures considered, homogeneous nucleation would require RHi values of approximately 140–150%, increasing with decreasing temperature. In the simulations, efficient DIN reduces RHi before this threshold is reached, effectively suppressing homogeneous freezing. As a result, homogeneous freezing does not contribute to the ICNC in this study (except when N_D is lower than measured concentration). For example, in the BASE simulation (Fig. 13a), large-scale ascent increases RHi up to about 110% below 9 km (SEDI), but sedimentation from above and in-situ ice formation limit further increase in RHi, preventing the onset of homogeneous freezing. Within the CONV layer, DIN maintains RHi near

https://doi.org/10.5194/egusphere-2026-2427
Preprint. Discussion started: 12 May 2026

saturation over ice due to large ice nucleation active dust particles.

3.2 Sensitivity simulations

3.2.1 Sensitivity to dust number concentration

Here, we discuss the impact of mineral dust number concentration N_D to the convection generation in dusty cirrus by varying the N_D within range of $N_D = 0.01 - 10\ \mathrm{cm}^{-3}$. Figure 11 shows the particle size distribution (PSD) of aerosols and ice crystals (ISD) simulated using the H14 scheme compared against in-situ observations at 9.5 km altitude. As we

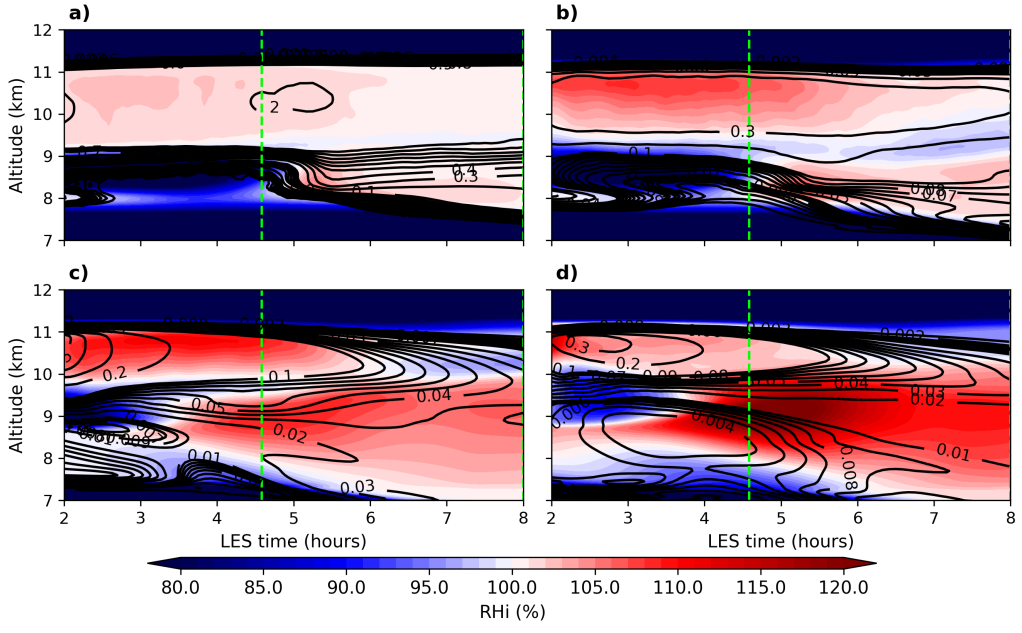

Figure 13. RHi (shading) and ICNC (contours, cm^{-3}) within the cirrus for different initial N_D in descending order a-d. The green dashed vertical line indicates the onset of SW radiation.

already discussed, mineral dust concentrations ($N_D \approx 10\ \mathrm{cm}^{-3}$) consistent with observations produce ICNC and ice size distributions (ISD) that are in good agreement with measurements at 9.5 km (underestimation below 9 km, as discussed in Sect. 3.1.2), with DIN dominating the ice formation when using the H14 scheme. Under these conditions, continuous production of small ice crystals is sustained, maintaining elevated number concentrations below 50 µm and supporting the observed cloud structure.

As N_D is reduced toward climatological mid-latitude values (Froyd et al., 2022), the ICNC decreases and the mode of the ISD shifts toward larger particle sizes. This reduction in N_D leads to insufficient ice production to sustain the observed cloud properties. In particular, for $N_D \leq 0.1\ \mathrm{cm}^{-3}$ cases, the ICNC decreases quickly after the spin up period, causing

https://doi.org/10.5194/egusphere-2026-2427
Preprint. Discussion started: 12 May 2026

weaker LW cooling at the cloud top (Fig. 13), and the increase in SW radiation intensity leads to collapse of the convective structure. Consequently, the cloud structure transitions from well-defined convective cells to a regime dominated by shear-induced perturbations in vertical velocity, indicating loss of persistence as shown in the Fig. 9. In cases where the convection was sustained until the end of the simulation runs ($N_D \geq 1\ \mathrm{cm}^{-3}$), structural differences are visible; with $N_D = 10\ \mathrm{cm}^{-3}$ (BASE) the cloud covered area is relatively homogeneous with small clear gaps in-between the cells, while at $N_D = 1\ \mathrm{cm}^{-3}$ the cells are more separated with weaker vertical velocity gradients, reflected in reduced ICNC. At sufficiently low N_D, homogeneous freezing begins to compensate for the reduced availability of INPs. This is reflected in increased mean RHi within the cirrus layer as N_D decreases (Fig. 13). However, while homogeneous freezing stabilizes ICNCs to some extent, it does not produce ICNC or ISDs comparable to observations, and is insufficient to sustain the convective structure of the cloud under the influence of SW radiation.

The quantitative relationships between the N_D and bulk cirrus properties at the end of the simulations are summarized in Fig. 14. ICNC increases approximately exponentially for $N_D > 0.1\ \mathrm{cm}^{-3}$. At lower concentrations ($N_D \approx 0.01$–$0.1\ \mathrm{cm}^{-3}$), ICNC shows weak sensitivity to N_D, as the remaining ice is largely residual from decaying convective structures rather than actively sustained nucleation. The IWC on the other hand does not seem to respond similarly to the N_D as the ICNC.

The dynamical response is also reflected in the N_D–stability relationship where the equivalent potential temperature gradient ($\partial\theta_e/\partial z$) provides a physically consistent diagnostic for dusty cirrus persistence as it shows whether the dusty cirrus layer can sustain its continuous generation of new convective cells and thus nucleation of new ice crystals. For $N_D \geq 1\ \mathrm{cm}^{-3}$, $\partial\theta_e/\partial z$ is in the negative range of values, indicating that radiative cooling is sufficient to generate conditional instability while for $N_D < 1\ \mathrm{cm}^{-3}$, the $\partial\theta_e/\partial z$ becomes positive, supporting the idea presented in the Fig. 9 that the generation of new convective cells is not sustained. The smaller the value of $\partial\theta_e/\partial z$ that seems to be below 0, the higher also are the vertical velocity fluctuations (σ_w) as shown in Fig. 14.

Additionally, since the INAS-based parameterizations used in this study determine the frozen fraction of particles based on their surface area, larger particles may contribute disproportionately to ICNC. Figure 15 shows the predicted INP particle size distribution calculated using Hiranuma et al. (2014) at 218 K for two RHi levels (105% and 120%). At higher RHi, submicrometer particles dominate the INP population, whereas at lower RHi, contributions from submicrometer and supermicron particles are more comparable. In contrast, supermicron particles appear relatively insensitive to RHi and activate at similar concentrations across both conditions. As shown in Fig. 14c, RHi values of 120% correspond to the upper range within the model domain, while the standard deviation of RHi is only $\sigma_{\mathrm{RHi}} = 4$–5%. This indicates that conditions closer to RHi = 105% occur more frequently. Consequently, the dust mass concentration becomes also an important predictor for dusty cirrus persistence. When expressed in terms of mass concentration rather than number concentration N_D (Fig. 14), the threshold for sustained cirrus is approximately $c_d \approx 6\ \mu\mathrm{g\,kg}^{-1}$ (integrated over particle diameters $D_p = 0.25$–$6\ \mu\mathrm{m}$), as shown in Supplementary Fig. S2.

As noted above, the DIN activity in this study scales with surface area which is the reason why larger dust particles preferably activate into ice. However, if DIN activation in fact scales less strongly, as suggested e.g by the experimental

https://doi.org/10.5194/egusphere-2026-2427
Preprint. Discussion started: 12 May 2026

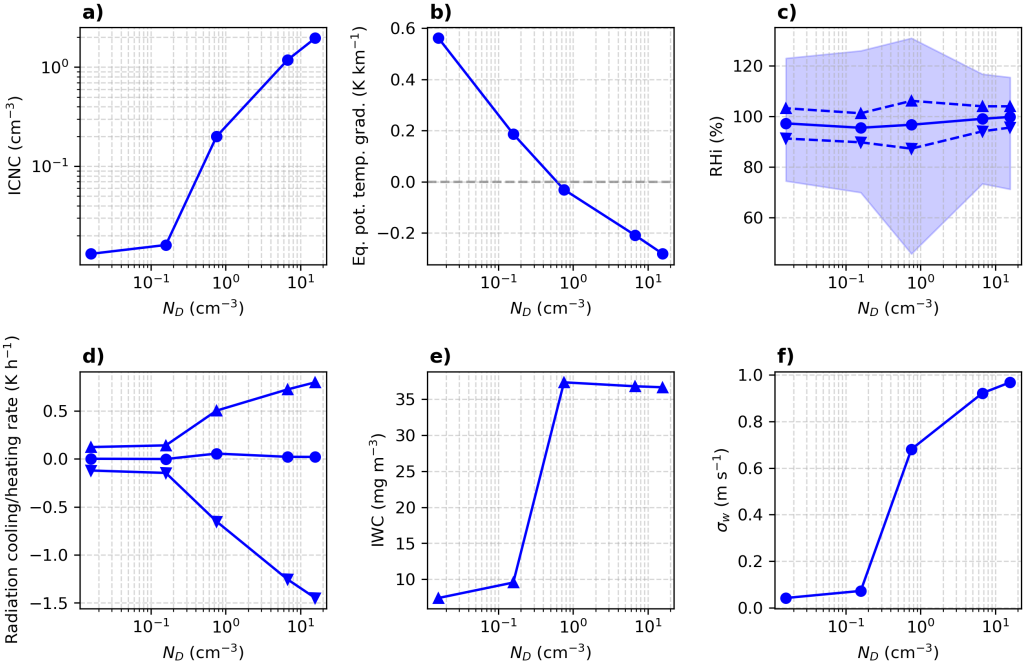

Figure 14. N_D (above 100 nm) versus mean ICNC a) minimum equivalent potential gradient (stability) b) range of RHi c) Radiative cooling/heating d) mean IWC e) and maximum standard deviation of w f). RHi is shown with with standard deviation and shaded area shows the absolute range of values. Radiation cooling/heating term represents the maximum flux at the cloud top for LW radiation (down triangles), SW radiation (up triangles) and net radiative term (circles). The statistics represent UCLALES-SALSA output in CONV (9.5-11 km). The N_D corresponds to initial concentration at the beginning of simulations between 8.5 and 11 km altitude.

results of Welti et al. (2009), ice nucleation could occur more effectively on smaller, sub-500 nm dust particles, compared to what current INAS formulations predict. In that case a higher ICNC could be expected that maintains dusty cirrus convection even with lower overall N_D.

We demonstrated here that accurately representing dust number and mass equally is essential for simulating dusty cirrus evolution because current parameterizations for DIN predict ice nucleation based on surface area scaling. Once convection is established at sufficiently high N_D, LW cooling at cloud top exceeds SW heating by nearly a factor of two at peak values (Fig. 14), highlighting the strong radiative-cooling potential of dusty cirrus clouds.
RHi also exhibits a dependence on N_D, where the RHi variability within the CONV decreases as N_D is increased, meaning that RHi is suppressed by frequent DIN events. The impact of radiation on dusty cirrus evolution is discussed more in depth in the following section.

https://doi.org/10.5194/egusphere-2026-2427
Preprint. Discussion started: 12 May 2026

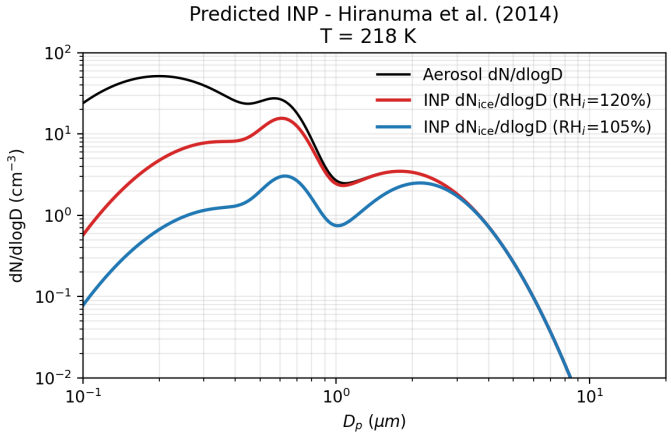

Figure 15. Predicted INP PSD calculated using the Hiranuma et al. (2014) based DIN activity of mineral dust particles shown at fixed temperature and two RHi levels.

3.2.2 Sensitivity to SW radiation and large-scale forcing

The simulated dusty cirrus represents essentially a snapshot of a mature dusty cirrus, and to extend this analysis, additional sensitivity experiments were performed to examine how solar radiation and large scale vertical velocity modulate the life cycle of dusty cirrus. The simulations include both nighttime and daytime conditions representative of 4 April, together with idealized large-scale vertical forcing scenarios, thus covering the whole diurnal cycle behavior.

Two simulations representing nighttime and daytime simulations are run with only radiation controlling evolution. Additionally, 4 simulations were conducted using a Gaussian vertical velocity forcing profile with peak magnitudes of ± 5 cms^{-1} under daytime and nighttime conditions. The forcing is strongest in the lower half of the cirrus layer and decreases toward the tropopause, consistent with the ERA5-derived structure used in the BASE case (Fig. 1). Daytime simulations were run for 16 hours to capture the full daylight cycle, while nighttime simulations were run for 8 hours. Horizontal wind nudging was disabled, as the objective here is not case-specific comparison but process-level understanding of cirrus persistence. An additional experiment was performed using the aerosol radiation scheme (AERORAD) with the BASE configuration to find whether dust-radiation interaction can have influence on the instability inside dusty cirrus clouds.

We first compare simulations without large-scale forcing. Under nighttime conditions (Fig. 16a), the dusty cirrus evolves only weakly over time. ICNC, RHi, and radiative fluxes remain nearly constant, and the cloud layer gradually ascends due to persistent LW cooling near the cloud top. In contrast, the daytime simulation (Fig. 16b) exhibits pronounced temporal evolution driven by increasing SW radiation after sunrise. During the early daytime hours, the cloud properties remain similar to the nighttime case, as SW heating is still weak. The two simulations start to diverge after approximately four hours, when the SW heating intensifies and reduces the net radiative cooling at the cloud top. The

https://doi.org/10.5194/egusphere-2026-2427
Preprint. Discussion started: 12 May 2026

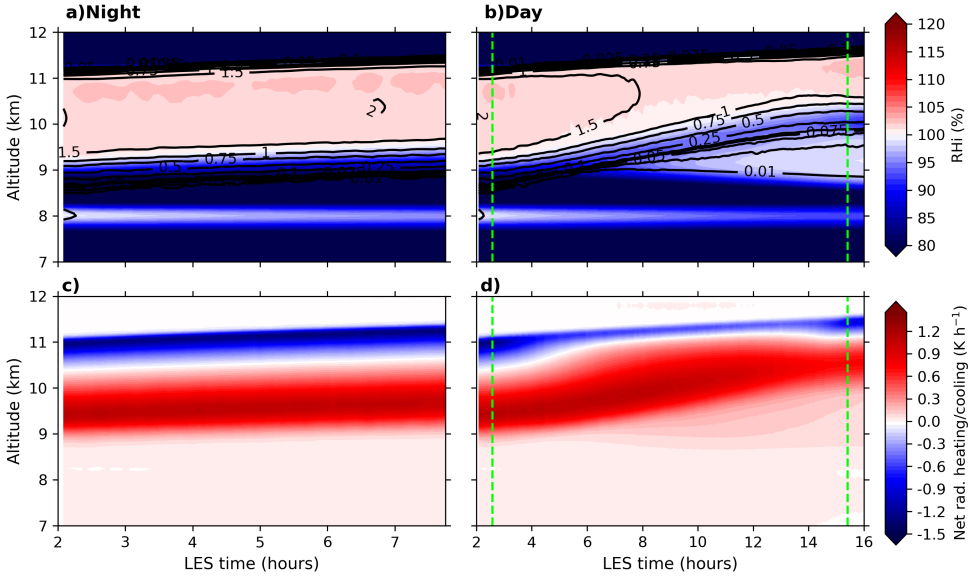

Figure 16. Night (a,c) and daytime (b,d) cases RHi in shading and ICNC (cm^{-3}) in contours in the upper panels. The lower panels show the corresponding net radiative heating/cooling rate. The day case is run for the whole day solar cycle where the downwelling SW radiation at the beginning and at the end of the simulation is close to 0. The vertical dashed line on the left in panels b) and d) indicates the time at which solar radiation induces a positive SW flux at the top of the model domain and the second line indicates zero SW flux at sunset.

weakened cooling at the cloud top results in weaker convection which shows as decreasing ICNC at the bottom of CONV. Peak SW heating occurs around hour 8 (solar noon), with mean heating rates of approximately 0.8 K h^{-1}. At this stage, LW cooling remains strong at about -1.4 K h^{-1}, so net cooling of -0.5 K h^{-1} persists at cloud top. However, SW absorption progressively alters the vertical structure of the cloud. Heating extends deeper into the cirrus layer and increases temperatures especially near 10 km altitude. This warming reduces RHi, since higher vapor content is required to maintain saturation. As a result, the cirrus layer contracts from below, and the cloud base rises by nearly 1 km by the end of the simulation.

Based on the daytime simulation results in Fig. 16b, the impact of SW radiation is self-limiting. As RHi decreases, both the ice nucleation and the depositional growth of the ice crystals weaken, reducing the IWC and ICNC. By the time of peak solar irradiance, the mean ICNC within the dusty cirrus decreases from a peak of 3 cm^{-3} to around 1.5 cm^{-3} (about 50% drop), which in turn diminishes both LW and SW radiative effects. The ICNC drop continues until the final hour of SW radiation (hour 14), with a three fold decrease from the peak ICNC.

The impacts of SW radiation found in this study are consistent with previous findings that cirrus layers tend to destabilize under LW cooling at night and stabilize under SW heating during daytime (Nagy, 2009; Kollath, 2010). Despite the strong influence of SW heating, the dusty cirrus impressively manages to sustain itself and even starts to re-intensify

https://doi.org/10.5194/egusphere-2026-2427
Preprint. Discussion started: 12 May 2026

after the SW heating ceases after sunset, as shown in Fig. 16 where the net radiative cooling intensifies between hours 14 and 16, resulting in stronger convection and higher ICNC. DARDAR-ice observations at 12 UTC show maintained high ICNC and IWC (corresponding to hour 10 in LES time (Fig. 10)), which indicates that the dusty cirrus convection was still sustained under the peak SW radiation as the model results also show. Also, since the model results suggest that ICNC decreases under SW heating, the DARDAR-ice perhaps would have measured higher ICNC if the overpass timing occurred earlier in the morning hours. Satellite observations from SEVIRI in Fig. 18 also show relatively cold cloud tops at this time, although warming is evident later in the afternoon, suggesting partial weakening of convection, agreeing with the model results. The SW radiation clearly affects the whole dusty cirrus covering large area over Europe in a similar manner with relatively uniform warming in mean brightness temperatures from around 210 K at night to increasing up to 220 K late in the afternoon. The influence of SW radiation seems to accelerate significantly after 12 UTC when the SW radiation is peaking. However, because of the cumulative effect that SW radiation has on the dusty cirrus convection based on the simulation results, this increasing trend confirms that the model represents the processes quite impressively. On top of that, the satellite observations also show the re-intensification of dusty cirrus after the sunset with increased occurrence of brightness temperatures found below 210 K. The model based cloud effective temperatures also shown in Fig. 18 indicate that at 12 UTC, the dusty cirrus was still sustaining its cold effective temperatures. Cloudsat overpass later in the afternoon might have measured substantially weakened dusty cirrus convective structures with lower ICNC values.

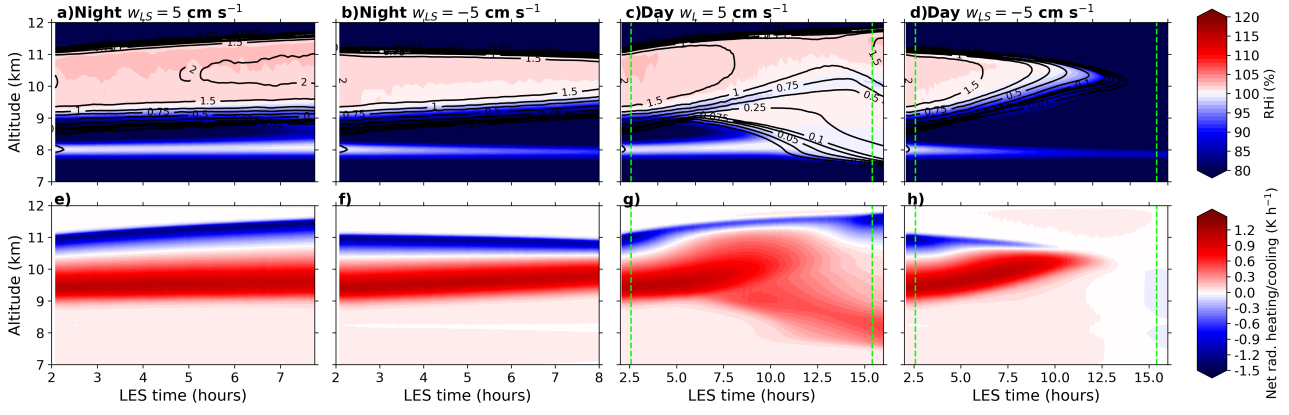

Figure 17. RHi in shading and ICNC (cm^{-3}) in contours (a-d) and net radiative heating rate in shading (e-h). Panels a) and b) represent nighttime simulations with $w_{LS} = 5$ cms^{-1} a) and $w_{LS} = -5$ cms^{-1} b). The same applies respectively for g) and h) in daytime simulations.

The role of large-scale forcing is illustrated in Fig. 17. Under upward forcing of 5 cms^{-1}, the dusty cirrus remains resilient to SW warming. The imposed ascent maintains supersaturation and sustains continuous ice nucleation. The resulting cirrus layer becomes vertically thicker, distributing LW heating more evenly and keeping net heating rates

https://doi.org/10.5194/egusphere-2026-2427
Preprint. Discussion started: 12 May 2026

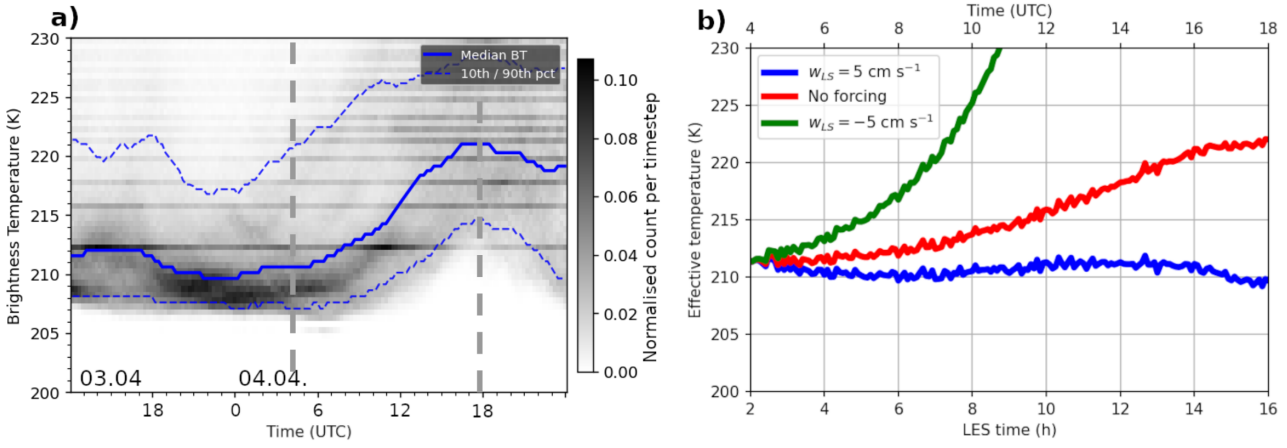

Figure 18. Temporal distribution from 03.04. 12 UTC to 05.04. 00 UTC of estimated brightness temperatures from SEVIRI MSG for 8.7µm retrieval a) and model output based effective temperatures in the model domain representing the daytime model runs b). Vertical dashed grey lines in a) indicates LES simulation times between 04 and 18 UTC.

smaller than without forcing. These results demonstrate that the vertical extent of the cirrus layer strongly influences its radiative balance, with thicker layers favoring smaller heating rates. The influence of upward forcing is also visible in the cloud effective temperatures (CET, comparable to cloud brightness temperatures measured by SEVIRI) (Fig. 18), as the CETs increase slightly towards the late afternoon and then either plateau at 220 K or decrease back to the 210 K level. The cooling caused by the large scale forcing seems to counterbalance the SW absorption induced warming and results in limited warming of CETs.

In contrast, subsidence forcing of $w_{LS} = -5$ cms^{-1} leads to fast decay of the dusty cirrus. Convective structures persist for a few hours before collapsing. The response closely resembles the effect of strong SW heating, with decreasing RHi and reduced ice production. In this case, subsidence also lowers RHi at the cloud top, further suppressing convective activity. In contrast at nighttime conditions and with subsidence applied, the dusty cirrus similarly shrinks in cloud layer thickness, however, because the SW radiation does not influence the net radiative cooling at the cloud top, the dusty cirrus maintains its convective structure relatively intact, without the feedback loop collapsing. Subsidence experiments show that under nighttime conditions, dusty cirrus can retain its properties even under moderate subsidence lasting for multiple hours consecutively. At day, the dusty cirrus, however, is significantly more influenced by the large scale forcing due to SW radiation.

Overall, based on the sensitivity simulation results, we find that SW radiation can suppress the ice nucleation and weaken the convective structure of dusty cirrus. Also, as was shown in Sect. 3.2.1, if N_D is considerably lower than the OPC measured N_D, the convective structure of the cirrus collapses due to the influence of SW absorption. The influence of aerosol–radiation interactions is shown in Fig. 19. The direct radiative effect of mineral dust within the cirrus is relatively weak. SW heating within the CONV increases by around 10-20% (0.01–0.04 K h^{-1}) when aerosol radiation is included.

https://doi.org/10.5194/egusphere-2026-2427
Preprint. Discussion started: 12 May 2026

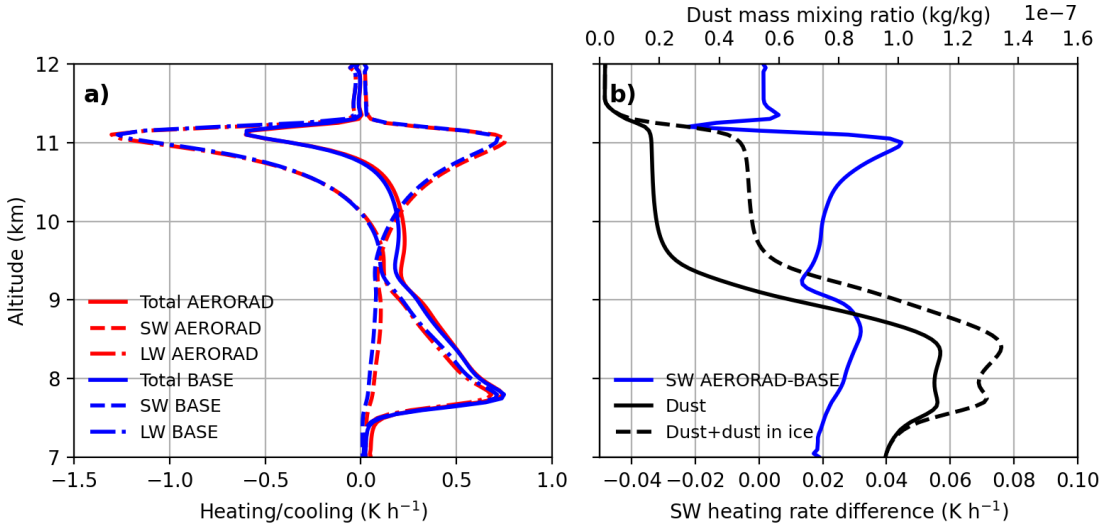

Figure 19. Panel a) shows aerosol radiation scheme (AERORAD) influence on heating term vertical profile from LW and SW heating rates compared with BASE run using H14 scheme without aerosol radiation. Panel b) illustrates the SW heating rate absolute difference AERORAD-BASE profile with dust mixing ratio vertical profile.

Larger effects are found below 9 km, where SW heating increases by up to 60%, consistent with higher dust mass mixing ratios at lower altitudes, although the SW flux is significantly smaller, meaning that the absolute difference in heating rates is at similar level inside CONV. Within the CONV layer, a large fraction of dust is incorporated into ice crystals, limiting its direct radiative impact. As a result, aerosol absorption plays only a secondary role in modulating cirrus dynamics compared to radiative cooling and large-scale forcing.

To summarize, the simulations show that dusty cirrus is most effectively maintained under nighttime conditions and in the presence of neutral or upward large-scale forcing. Strong SW radiation and subsidence both act to suppress convection. Dusty cirrus can sustain its structure even under solar noon, although with reduced cirrus layer depth.

4 Conclusions

In this study, the conditions governing dusty cirrus persistence were investigated with Large-Eddy Simulator UCLALES-SALSA model using data from ML-CIRRUS campaign flight that sampled these clouds. Previous regional scale model studies have shown that the interaction between mineral dust, humidity, and radiative fluxes is central to dusty cirrus evolution and to their radiative impact, including implications for solar energy production (e.g. Weger et al., 2018; Seifert et al., 2023) while lacking the ability to explain the microphysical aspects controlling dusty cirrus due to the lack of sufficiently high resolution to simulate the convection directly. In this study, these processes were explicitly resolved, which provided a more complete representation of the dynamics and microphysical aspects of the dusty cirrus.

https://doi.org/10.5194/egusphere-2026-2427
Preprint. Discussion started: 12 May 2026

Sensitivity experiments varying the concentration of mineral dust showed that sustained convective cirrus development requires mineral dust number and mass concentrations that exceed climatological values by approximately one to two orders of magnitude to result in persistent cirrus convection even during the day, with the threshold concentration found at $N_D = 1$ cm^{-3} (in terms of mass at $c_d = 6$ μg kg^{-1}). Under these conditions, heterogeneous ice nucleation can maintain a sufficiently high ICNC to preserve strong longwave cooling at the cloud top (as proposed in Weger et al. (2018) and Seifert et al. (2023)), which in turn sustains conditional instability and convective overturning. When dust concentrations are lower, ice production weakens, longwave radiative cooling becomes insufficient to maintain instability, and the convective organization of the cloud decays. Shortwave radiation exerts a strong modulation on this feedback loop. Longwave cooling promotes instability maintenance and helps to support convective circulation, whereas shortwave radiative heating counteracts this process with opposite heating term to longwave cooling at the cloud top to reduce convective mixing that results in suppressed ice formation during daytime. The radiation sensitivity simulations showed that dusty cirrus is most stable under nighttime conditions, when longwave cooling dominates. During the day, the dusty cirrus can still persist if dust concentrations remain high enough inside the cirrus. In contrast, subsidence and strong shortwave heating both act to weaken or collapse the convective structure.

The modeled cirrus properties were also found to be highly sensitive to the choice of deposition ice nucleation (DIN) parameterization scheme. Hiranuma et al. (2014), Ullrich et al. (2017) and Phillips et al. (2013) schemes produced substantially different ice nucleation efficiencies and vertical distributions of ICNC, which altered the dynamical and radiative evolution of the dusty cirrus. This sensitivity highlights an important source of uncertainty in modeling of dusty cirrus and points to the need for improved constraints on heterogeneous ice nucleation on mineral dust in cirrus regime temperatures where mineral dust dominates in heterogeneous freezing. The observed sensitivity also suggests that dusty cirrus events provide a useful test bed for evaluating DIN parameterizations. Improved observational constraints, especially from targeted in-situ campaigns, are therefore needed to reduce uncertainty in the simulation of dusty cirrus systems and their climatic impact. Because we considered only a single input temperature profile for ice formation, the full temperature range over which dusty cirrus evolution is sustained remains unknown. A more comprehensive assessment would require simulations spanning a wider range of temperature conditions.

Homogeneous freezing, on the other hand, was not found to contribute to ice nucleation when the parameterization of Hiranuma et al. (2014) was used with mineral dust concentrations similar to those measured with OPC. Homogeneous freezing had a marginal contribution to freezing when dust concentration was lowered by a magnitude, also corresponding to the case where dusty cirrus convection was barely sustained while it did not collapse under shortwave radiation heating.

In summary, the results show that the persistence of dusty cirrus emerges from coupled feedback between dust-driven DIN, longwave radiative cooling, and convective dynamics. The simulations further indicate that shortwave heating, large-scale vertical motion, and DIN representation exert important controls on the lifecycle of the dusty cirrus.

https://doi.org/10.5194/egusphere-2026-2427
Preprint. Discussion started: 12 May 2026

Data availability. ML-CIRRUS (NIXE-CAPS, OPC, BAHAMAS) measurements and data products are provided via the HALO database (HALO consortium, 2017). The MIRA-35C data used in this study are generated by the Aerosol, Clouds and Trace Gases Research Infrastructure (ACTRIS) and are available from the ACTRIS Data Centre using the following link: https://hdl.handle.net/21.12132/1.cd92913b0b6e4625. Simulation data used for analysis is archived at Zenodo (https://doi.org/10.5281/zenodo.19824432; Juurikkala et al. (2026)). The source code of the model UCLALES-SALSA is available from GitHub at https://github.com/UCLALES-SALSA/ UCLALES-SALSA under release tag dustycirrus.

Author contributions. KJ made the simulations, analysed the simulation results and wrote major parts of the text. TR supported data analysis interpretation and editing of the text. MK provided the campaign data and helped to interpret in-situ data. CW supported with interpretation of in-situ measurements and model simulations, and text editing. AL supervised the project and provided guidance on the manuscript.

Competing interests. Some authors are members of the editorial board of Atmospheric Chemistry and Physics.

Acknowledgements. This work was supported by grant by Emil Aaltonen foundation (grant no. 250052 K1), the Academy of Finland Flagship ACCC (grant no. 337552) and MEDICEN project (grant no. 345125), and the European Union's Horizon Europe Clean-Cloud project (grant agreement no. 101137639). We acknowledge ACTRIS for providing the data sets. We acknowledge EUMETSAT for providing MSG SEVIRI data. We also thank Daniel Sauer from DWD for providing OPC data. We give special thanks to Sami Romakkaniemi and Silvia Cadéron at FMI for supporting with model specific aspects.

https://doi.org/10.5194/egusphere-2026-2427
Preprint. Discussion started: 12 May 2026

Appendix A: Dusty cirrus diagnostics

A1 Equivalent potential temperature

For diagnostics for convection within the model domain, we use the equivalent potential temperature which is conserved in phase-transition between ice and vapor and is generally acceptable to use under the conditions in this study where temperatures are below 235 K (Spichtinger, 2014). The equivalent potential temperature is described as:

$$\theta_e = T\left(\frac{p_0}{p}\right)^{\frac{R}{c_p}} \exp\left(\frac{L_s q}{c_p T}\right) \tag{A1}$$

A2 Temperature tendency equation

In this study, we focus on the thermodynamic heating rates within the simulated cloud, with the aim of identifying the processes that control the evolution of the temperature profile in the model domain. The prognostic temperature tendency can be decomposed into contributions from radiation, latent heating, turbulent mixing, and large-scale forcing as follows:

$$\underbrace{\frac{\partial T}{\partial t}}_{\text{Total heating rate}} = \underbrace{-\left(\frac{\partial F_{SW}}{\partial z} - \frac{\partial F_{LW}}{\partial z}\right)\frac{1}{c_p \rho_a}}_{\text{Radiation}} \underbrace{- \frac{L_s}{c_p}\frac{\partial q}{\partial t}}_{\text{Latent heat}} \underbrace{- \frac{\partial \overline{w'\theta'}}{\partial z}}_{\text{Turbulent mixing}} \underbrace{- w_{LS}\frac{\partial \theta}{\partial z}\frac{T}{\theta}}_{\text{Large scale forcing}} \tag{A2}$$

A3 Cloud effective temperature

The cloud effective temperature based on the UCLALES-SALSA output was calculated using a simple formulation:

$$T_{eff} \approx \left(\frac{F_{LW\uparrow}}{\sigma}\right)^{1/4} \tag{A3}$$

that assumes that the cirrus emits black body radiation. σ represents the Stefan-Bolzmann constant and $F_{LW\uparrow}$ the upwelling LW radiation at the top of the model domain. We also assumed that the dusty cirrus has a high optical depth $\tau \gg 1$ and thus can be assumed to leak minimal background radiation from the ground. Under the assumed conditions, the cloud effective temperature is roughly equal to the SEVIRI MSG based estimation of brightness temperatures for 8.7 µm.

Appendix B: Ice nucleation parameterizations

B1 Hiranuma et al. (2014) ice nucleation parameterization

The heterogeneous ice nucleation parameterization of Hiranuma et al. (2014) is based on laboratory measurements conducted in the AIDA cloud chamber, where ice formation on hematite particles was investigated under cirrus-relevant conditions. Hematite was used as a proxy for mineral dust, and experiments were performed over a wide temperature

https://doi.org/10.5194/egusphere-2026-2427
Preprint. Discussion started: 12 May 2026

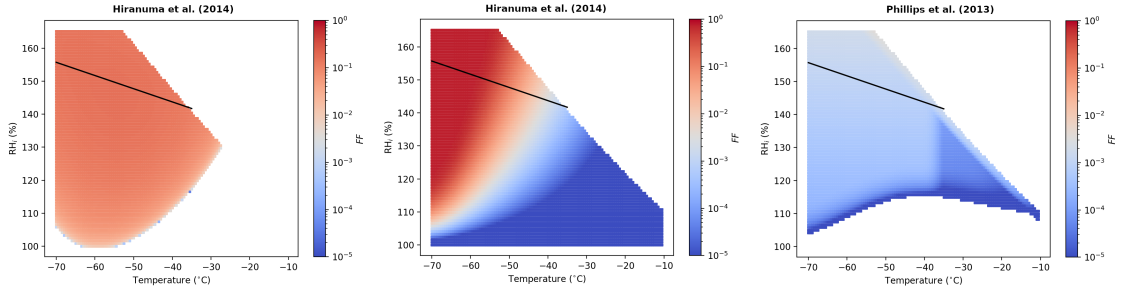

Figure B1. Frozen fraction (FF) calculated based on the aerosol PSD shown in Fig. 5 with Hiranuma et al. (2014, H14), Ullrich et al. (2017, U17) and Phillips et al. (2013, P13) scheme in deposition nucleation conditions. Solid black line indicates the Koop et al. (2000) threshold line for onset of homogeneous freezing.

range (-36 to -78 °C) under water-subsaturated conditions by varying temperature (T) and relative humidity with respect to ice (RH_i). These measurements provide a consistent dataset for deriving ice nucleation activity under controlled thermodynamic conditions.

The parameterization follows the ice nucleation active surface site (INAS) density framework, in which the number of ice-active sites per unit particle surface area, n_s, is expressed as a function of temperature and ice supersaturation. The number concentration of activated ice nucleating particles (INP) is then given by

$$n_{\mathrm{INP}} = N_{\mathrm{aer}} \left(1 - \exp\left[-n_s(T, RH_i) \cdot A_{\mathrm{aer}}\right]\right), \tag{B1}$$

where N_{aer} is the aerosol number concentration and A_{aer} is the particle surface area.

The core of the parameterization is the empirical formulation of the surface site density n_s, which depends on both temperature and ice supersaturation. The parameterization distinguishes different temperature regimes, reflecting the experimentally observed variation in nucleation pathways:

$$n_s = f(T, RH_i), \tag{B2}$$

where $f(T, RH_i)$ is derived from AIDA measurements. In practice, n_s is expressed as an exponential function of RH_i and/or T, with different coefficients depending on the temperature range.

In general form, the parameterization can be expressed as

https://doi.org/10.5194/egusphere-2026-2427
Preprint. Discussion started: 12 May 2026

$$
\begin{aligned}
n_s(T, RH_i) = & -3.777 \times 10^{13} - 7.818 \times 10^{11} \cdot T + 4.252 \times 10^{11} \cdot RH_i \\
& - 4.598 \times 10^{9} \cdot T^2 + 6.952 \times 10^{9} \cdot T \cdot RH_i - 1.111 \times 10^{9} \cdot RH_i^2 \\
& - 2.966 \times 10^{6} \cdot T^3 + 2.135 \times 10^{7} \cdot T^2 \cdot RH_i \\
& - 1.729 \times 10^{7} \cdot T \cdot RH_i^2 - 9.438 \times 10^{5} \cdot RH_i^3
\end{aligned} \tag{B3}
$$

This formulation is valid within the range

$$
-78^{\circ}\mathrm{C} < T < -36^{\circ}\mathrm{C}, \quad 100\% < RH_i < RH_{\mathrm{water}}. \tag{B4}
$$

where the coefficients are empirically fitted to the AIDA measured data.

The number of INPs can be calculated by multiplying the INAS density by the surface area of the particle as

$$
n_{\mathrm{INP}}(T, RH_i) = 1 - \exp(-n_s S_{\mathrm{dust}}) \tag{B5}
$$

B2 Ullrich et al. (2017) ice nucleation parameterization

The Ullrich et al. (2017) parameterization scheme for deposition ice nucleation is based on 11 years worth of laboratory experiments conducted in the Aerosol Interaction and Dynamics in the Atmosphere (AIDA) chamber. This framework was specifically developed to assess the nucleation characteristics of mineral dust and soot particles under conditions relevant to cirrus clouds (Ullrich et al., 2019). The parameterization presented below quantifies the nucleation ability of mineral dust/soot particles in terms of ice nucleation active site (INAS) density n_s (e.g., Hoose and Möhler, 2012; Vali et al., 2015). The parameterization is given by:

$$
n_s = \exp\{\alpha(RH_i - 100)^{1/4} \cos[\beta(T - \gamma)]^2 \mathrm{arccot}[\kappa(T - \lambda)]/\pi\} \tag{B6}
$$

where the parameters and corresponding values for mineral dust are given in Table B1.

	α	β	γ	κ	λ	Valid temperature range (K)
Mineral dust	285.692	0.017	256.692	0.080	200.745	[206, 240]

Table B1. Fit parameters for equation 2.11 for mineral dust particles. The parameterization is valid for S_i below water saturation, homogeneous nucleation threshold and above 1.0.

B3 Phillips et al. (2013) ice nucleation parameterization

The heterogeneous ice nucleation parameterization presented in Phillips et al. (2008), with updates described in Phillips et al. (2013), is an empirical framework based on a combination of in-situ field measurements and laboratory data of ice-nucleating particles (INPs) in the troposphere. The formulation links ice nucleation activity to aerosol physicochemical

https://doi.org/10.5194/egusphere-2026-2427
Preprint. Discussion started: 12 May 2026

properties, particularly particle surface area and composition, and accounts for variability across different aerosol species (Phillips et al., 2008).

In this framework, aerosol particles are divided into distinct classes (e.g., mineral dust, black carbon, and organic or biological particles), and the total number concentration of nucleated ice crystals is obtained as the sum of contributions from each species. The parameterization assumes that ice nucleation activity scales with aerosol surface area and depends on both temperature T and RHi. For each aerosol type, the activated INP concentration is expressed as

$$n_{\mathrm{INP},X} = 1 - \exp(-\mu_{\mathrm{X}}(D_X, T, RH_i)), \tag{B7}$$

where n_X is the aerosol number concentration and μ_X is the mean number of ice embryos per insoluble particle of size D_X. This term encapsulates the probability of ice nucleation and depends on RHi and temperature.

The functional dependence of μ_X is given by

$$\mu_X = H_X(S_i, T)\,\xi(T)\,\frac{\alpha_X n_{\mathrm{IN},1,*}}{\Omega_{X,1,*}}\pi D_X^2, \tag{B8}$$

where $H_X(S_i, T)$ describes the dependence on ice supersaturation and temperature, $\xi(T)$ accounts for temperature-dependent scaling of nucleation efficiency, α_X for the fractional contribution from aerosol group X to the INP concentration, and the ratio $\frac{n_{\mathrm{IN},1,*}}{\Omega_{X,1,*}}$ represents a reference activity of INPs in the background troposphere divided by INP total surface area between 0.1-1 µm (Phillips et al., 2008). In this study, we used simplified formulation where we used

$$n_{\mathrm{INP},1,^*}(T, RH_i) = c_1(\exp[12.96(RH_i - 110)])^{0.3}/\rho_a, \tag{B9}$$

which is applicable below the homogeneous freezing temperature threshold $T \leq -35°\mathrm{C}$ and $100 < RH_i \leq RH_i^{\mathrm{hom}}$.

The more recent version by Phillips et al. (2013) updated the existing parameterization framework with an onset temperature for freezing and baseline surface areas of aerosols observed in field campaigns, and accommodated more laboratory and field observations to its formulation. For a more detailed description of the parameterization scheme, see Phillips et al. (2008).

B4 Homogeneous freezing parameterization by Koop et al. (2000)

The parameterization for homogeneous freezing follows the formulation of Koop et al. (2000). The nucleation rate is parametrized with a shift in the melting curve of ice $\Delta a_w = a_w - a_w^i$. In Koop (2015), a simplication for a_w was presented as $a_w^i = S_i \frac{p_{\mathrm{ice,sat}}(T)}{p_{\mathrm{liq,sat}}(T)} = \frac{p_{\mathrm{v}}(T)}{p_{\mathrm{liq,sat}}(T)}$. From this, the equation follows:

$$\Delta a_w = a_w - a_w^i = \frac{p_v}{p_{\mathrm{liq}}(T)} - \frac{p_{\mathrm{ice}}(T)}{p_{\mathrm{liq}}(T)} \tag{B10}$$

https://doi.org/10.5194/egusphere-2026-2427
Preprint. Discussion started: 12 May 2026

The Koop et al. (2000) parameterizations produces the freezing rate ($\mathrm{cm}^{-3}\mathrm{s}^{-1}$) as:

$$\log(J_H H) = -906.7 + 8502\Delta a_w - 26924(\Delta a_w)^2 + 29180(\Delta a_w)^3 \tag{B11}$$

which results in a predicted frozen fraction FF based on the J_H:

$$FF = J_H S = J_H \pi D_d^3 \Delta t, \tag{B12}$$

where D_d represents the soluble droplet diameter and Δt time difference.

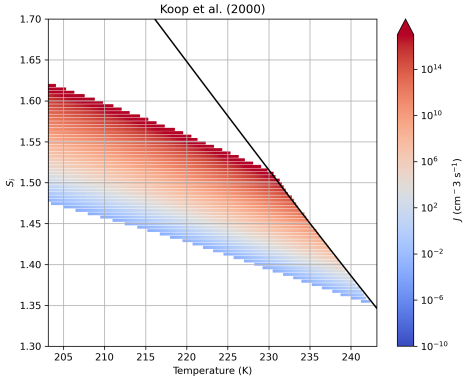

Figure B2. Koop et al. (2000) parameterization scheme as a function of temperature and Δa_w. The solid line indicates the water saturation line.

https://doi.org/10.5194/egusphere-2026-2427
Preprint. Discussion started: 12 May 2026

References

Ahola, J., Korhonen, H., Tonttila, J., Romakkaniemi, S., Kokkola, H., and Raatikainen, T.: Modelling mixed-phase clouds with the large-eddy model UCLALES–SALSA, Atmospheric Chemistry and Physics, 20, 11 639–11 654, https://doi.org/10.5194/acp-20-11639-2020, 2020.

Ansmann, A., Mamouri, R.-E., Bühl, J., Seifert, P., Engelmann, R., Hofer, J., Nisantzi, A., Atkinson, J. D., Kanji, Z. A., Sierau, B., Vrekoussis, M., and Sciare, J.: Ice-nucleating particle versus ice crystal number concentration in altocumulus and cirrus layers embedded in Saharan dust: a closure study, Atmospheric Chemistry and Physics, 19, 15 087–15 115, https://doi.org/10.5194/acp-19-15087-2019, 2019.

Calderón, S. M., Hyttinen, N., Kokkola, H., Raatikainen, T., Lawson, R. P., and Romakkaniemi, S.: Secondary ice formation in cumulus congestus clouds: insights from observations and aerosol-aware large-eddy simulations, Atmospheric Chemistry and Physics, 25, 14 479–14 500, https://doi.org/10.5194/acp-25-14479-2025, 2025.

Delanoë, J., Protat, A., Testud, J., Bouniol, D., Heymsfield, A. J., Bansemer, A., Brown, P. R. A., and Forbes, R. M.: Statistical properties of the normalized ice particle size distribution, Journal of Geophysical Research: Atmospheres, 110, https://doi.org/https://doi.org/10.1029/2004JD005405, 2005.

Ewald, F., Mattis, I., Zinner, T., and O'Connor, E. J.: Categorize data from Schneefernerhaus on 4 April 2014, https://hdl.handle.net/21.12132/1.cd92913b0b6e4625, 2026.

Fromm, M., Kablick III, G., and Caffrey, P.: Dust-infused baroclinic cyclone storm clouds: The evidence, meteorology, and some implications, Geophysical Research Letters, 43, 12,643–12,650, https://doi.org/https://doi.org/10.1002/2016GL071801, 2016.

Froyd, K., Yu, P., Schill, G., Brock, C., Kupc, A., Williamson, C., Jensen, E., Ray, E., Rosenlof, K., Bian, H., Darmenov, A., Colarco, P., Diskin, G., Bui, T., and Murphy, D.: Dominant role of mineral dust in cirrus cloud formation revealed by global-scale measurements, Nature Geoscience, 15, 1–7, https://doi.org/10.1038/s41561-022-00901-w, 2022.

Fu, Q. and Liou, K. N.: Parameterization of the Radiative Properties of Cirrus Clouds, Journal of Atmospheric Sciences, 50, 2008 – 2025, https://doi.org/10.1175/1520-0469(1993)050<2008:POTRPO>2.0.CO;2, 1993.

Fusina, F. and Spichtinger, P.: Cirrus clouds triggered by radiation, a multiscale phenomenon, Atmospheric Chemistry and Physics, 10, 5179–5190, https://doi.org/10.5194/acp-10-5179-2010, 2010.

Giez, A., Mallaun, C., Nenakhov, V., and Zöger, M.: Calibration of a Nose Boom Mounted Airflow Sensor on an Atmospheric Research Aircraft by Inflight Maneuvers, Tech. rep., ISSN 1434-8454, https://elib.dlr.de/145969/, 2021.

Gruber, S., Blahak, U., Haenel, F., Kottmeier, C., Leisner, T., Muskatel, H., Storelvmo, T., and Vogel, B.: A Process Study on Thinning of Arctic Winter Cirrus Clouds With High-Resolution ICON-ART Simulations, Journal of Geophysical Research: Atmospheres, 124, 5860–5888, https://doi.org/https://doi.org/10.1029/2018JD029815, 2019.

Hiranuma, N., Paukert, M., Steinke, I., Zhang, K., Kulkarni, G., Hoose, C., Schnaiter, M., Saathoff, H., and Möhler, O.: A comprehensive parameterization of heterogeneous ice nucleation of dust surrogate: laboratory study with hematite particles and its application to atmospheric models, Atmospheric Chemistry and Physics, 14, 13 145–13 158, https://doi.org/10.5194/acp-14-13145-2014, 2014.

Hogan, R. J., Mittermaier, M. P., and Illingworth, A. J.: The Retrieval of Ice Water Content from Radar Reflectivity Factor and Temperature and Its Use in Evaluating a Mesoscale Model, Journal of Applied Meteorology and Climatology, 45, 301 – 317, https://doi.org/10.1175/JAM2340.1, 2006.

https://doi.org/10.5194/egusphere-2026-2427
Preprint. Discussion started: 12 May 2026

Hoose, C. and Möhler, O.: Heterogeneous ice nucleation on atmospheric aerosols: a review of results from laboratory experiments, Atmospheric Chemistry and Physics, 12, 9817–9854, https://doi.org/10.5194/acp-12-9817-2012, 2012.

Illingworth, A. J., Hogan, R. J., O'Connor, E., Bouniol, D., Brooks, M. E., Delanoé, J., Donovan, D. P., Eastment, J. D., Gaussiat, N., Goddard, J. W. F., Haeffelin, M., Baltink, H. K., Krasnov, O. A., Pelon, J., Piriou, J.-M., Protat, A., Russchenberg, H. W. J., Seifert, A., Tompkins, A. M., van Zadelhoff, G.-J., Vinit, F., Willén, U., Wilson, D. R., and Wrench, C. L.: Cloudnet: Continuous Evaluation of Cloud Profiles in Seven Operational Models Using Ground-Based Observations, Bulletin of the American Meteorological Society, 88, 883 – 898, https://doi.org/10.1175/BAMS-88-6-883, 2007.

Juurikkala, K., Williamson, C. J., Froyd, K. D., Dean-Day, J., and Laaksonen, A.: Prior heterogeneous ice nucleation events shape homogeneous freezing during the evolution of synoptic cirrus, Atmospheric Chemistry and Physics, 25, 13 995–14 013, https://doi.org/10.5194/acp-25-13995-2025, 2025.

Juurikkala, K., Raatikainen, T., Williamson, C., Krämer, M., and Laaksonen, A.: Supplementary material for the ACP Manuscript, Mineral dust concentration controlling convective cirrus structure and persistence: a large-eddy simulation study with observational constraints, https://doi.org/10.5281/zenodo.19824432, 2026.

Kazil, J., Christensen, M. W., Abel, S. J., Yamaguchi, T., and Feingold, G.: Realism of Lagrangian Large Eddy Simulations Driven by Reanalysis Meteorology: Tracking a Pocket of Open Cells Under a Biomass Burning Aerosol Layer, Journal of Advances in Modeling Earth Systems, 13, e2021MS002 664, https://doi.org/https://doi.org/10.1029/2021MS002664, e2021MS002664 2021MS002664, 2021.

Koehler, K. A., Kreidenweis, S. M., DeMott, P. J., Petters, M. D., Prenni, A. J., and Möhler, O.: Laboratory investigations of the impact of mineral dust aerosol on cold cloud formation, Atmospheric Chemistry and Physics, 10, 11 955–11 968, https://doi.org/10.5194/acp-10-11955-2010, 2010.

Kokkola, H., Korhonen, H., Lehtinen, K. E. J., Makkonen, R., Asmi, A., Järvenoja, S., Anttila, T., Partanen, A.-I., Kulmala, M., Järvinen, H., Laaksonen, A., and Kerminen, V.-M.: SALSA – a Sectional Aerosol module for Large Scale Applications, Atmospheric Chemistry and Physics, 8, 2469–2483, https://doi.org/10.5194/acp-8-2469-2008, 2008.

Kokkola, H., Kühn, T., Laakso, A., Bergman, T., Lehtinen, K. E. J., Mielonen, T., Arola, A., Stadtler, S., Korhonen, H., Ferrachat, S., Lohmann, U., Neubauer, D., Tegen, I., Siegenthaler-Le Drian, C., Schultz, M. G., Bey, I., Stier, P., Daskalakis, N., Heald, C. L., and Romakkaniemi, S.: SALSA2.0: The sectional aerosol module of the aerosol–chemistry–climate model ECHAM6.3.0-HAM2.3-MOZ1.0, Geoscientific Model Development, 11, 3833–3863, https://doi.org/10.5194/gmd-11-3833-2018, 2018.

Kollath, K.: Cellular convection in cirrus clouds as a possible effect of dust aerosols, https://www.eumetsat.int/media/46886, eUMETSAT, last access: 30 October 2022, 2010.

Koop, T.: Atmospheric Water, in: Water: Fundamentals as the Basis for Understanding the Environment and Promoting Technology, edited by Debenedetti, P. G., Ricci, A., and Bruni, F., pp. 45–75, IOS Press, Amsterdam and Bologna, https://doi.org/10.3254/978-1-61499-507-4-45, 2015.

Koop, T., Luo, B., Tsias, A., and Peter, T.: Water Activity as the determinant for homogeneous ice nucleation in aqueous solutions, Nature, 406, 611–4, https://doi.org/10.1038/35020537, 2000.

Krautstrunk, M. and Giez, A.: The Transition From FALCON to HALO Era Airborne Atmospheric Research, pp. 609–624, Springer Berlin Heidelberg, Berlin, Heidelberg, ISBN 978-3-642-30183-4, https://doi.org/10.1007/978-3-642-30183-4_37, 2012.

https://doi.org/10.5194/egusphere-2026-2427
Preprint. Discussion started: 12 May 2026

Lamb, K. D., Harrington, J. Y., Clouser, B. W., Moyer, E. J., Sarkozy, L., Ebert, V., Möhler, O., and Saathoff, H.: Re-evaluating cloud chamber constraints on depositional ice growth in cirrus clouds – Part 1: Model description and sensitivity tests, Atmospheric Chemistry and Physics, 23, 6043–6064, https://doi.org/10.5194/acp-23-6043-2023, 2023.

Lawson, R. P., Woods, S., Jensen, E., Erfani, E., Gurganus, C., Gallagher, M., Connolly, P., Whiteway, J., Baran, A. J., May, P., Heymsfield, A., Schmitt, C. G., McFarquhar, G., Um, J., Protat, A., Bailey, M., Lance, S., Muehlbauer, A., Stith, J., Korolev, A., Toon, O. B., and Krämer, M.: A Review of Ice Particle Shapes in Cirrus formed In Situ and in Anvils, Journal of Geophysical Research: Atmospheres, 124, 10 049–10 090, https://doi.org/https://doi.org/10.1029/2018JD030122, 2019.

Meyer, J.: Ice Crystal Measurements with the New Particle Spectrometer NIXE-CAPS, vol. 160 of *Schriften des Forschungszentrums Jülich. Reihe Energie und Umwelt / Energy and Environment*, Forschungszentrum Jülich, Jülich, Germany, ISBN 9783893368402, 2012.

Minikin, A., Petzold, A., Ström, J., Krejci, R., Seifert, M., van Velthoven, P., Schlager, H., and Schumann, U.: Aircraft observations of the upper tropospheric fine particle aerosol in the Northern and Southern Hemispheres at midlatitudes, Geophysical Research Letters, 30, https://doi.org/https://doi.org/10.1029/2002GL016458, 2003.

Mitchell, D. L. and Heymsfield, A. J.: Refinements in the Treatment of Ice Particle Terminal Velocities, Highlighting Aggregates, Journal of the Atmospheric Sciences, 62, 1637 – 1644, https://doi.org/10.1175/JAS3413.1, 2005.

Möhler, O., Field, P. R., Connolly, P., Benz, S., Saathoff, H., Schnaiter, M., Wagner, R., Cotton, R., Krämer, M., Mangold, A., and Heymsfield, A. J.: Efficiency of the deposition mode ice nucleation on mineral dust particles, Atmospheric Chemistry and Physics, 6, 3007–3021, https://doi.org/10.5194/acp-6-3007-2006, 2006.

Murphy, D. M. and Koop, T.: Review of the vapour pressures of ice and supercooled water for atmospheric applications, Quarterly Journal of the Royal Meteorological Society, 131, 2005.

Nagy, A.: Investigating weather situations which bring Saharan dust over Hungary based on MSG satellite images, Master's thesis, ELTE University, 2009.

NASA: MODIS/Terra Atmospherically Corrected Surface Reflectance Product (MOD09), https://doi.org/10.5067/MODIS/MOD09.061, level-2 atmospheric-corrected surface reflectance (MOD09 series).

Ovchinnikov, M., Ackerman, A. S., Avramov, A., Cheng, A., Fan, J., Fridlind, A. M., Ghan, S., Harrington, J., Hoose, C., Korolev, A., McFarquhar, G. M., Morrison, H., Paukert, M., Savre, J., Shipway, B. J., Shupe, M. D., Solomon, A., and Sulia, K.: Intercomparison of large-eddy simulations of Arctic mixed-phase clouds: Importance of ice size distribution assumptions, Journal of Advances in Modeling Earth Systems, 6, 223–248, https://doi.org/https://doi.org/10.1002/2013MS000282, 2014.

Phillips, V., DeMott, P., and Andronache, C.: An Empirical Parameterization of Heterogeneous Ice Nucleation for Multiple Chemical Species of Aerosol, Journal of the Atmospheric Sciences, 65, 2757–2783, https://doi.org/10.1175/2007JAS2546.1, 2008.

Phillips, V. T. J., Demott, P. J., Andronache, C., Pratt, K. A., Prather, K. A., Subramanian, R., and Twohy, C.: Improvements to an Empirical Parameterization of Heterogeneous Ice Nucleation and Its Comparison with Observations, Journal of the Atmospheric Sciences, 70, 378 – 409, https://doi.org/10.1175/JAS-D-12-080.1, 2013.

Rieger, D., Steiner, A., Bachmann, V., Gasch, P., Förstner, J., Deetz, K., Vogel, B., and Vogel, H.: Impact of the 4 April 2014 Saharan dust outbreak on the photovoltaic power generation in Germany, Atmospheric Chemistry and Physics, 17, 13 391–13 415, https://doi.org/10.5194/acp-17-13391-2017, 2017.

Schumann, U., Mayer, B., Gierens, K., Unterstrasser, S., Jessberger, P., Petzold, A., Voigt, C., and Gayet, J.-F.: Effective Radius of Ice Particles in Cirrus and Contrails, Journal of the Atmospheric Sciences, 68, 300 – 321, https://doi.org/10.1175/2010JAS3562.1, 2011.

https://doi.org/10.5194/egusphere-2026-2427
Preprint. Discussion started: 12 May 2026

Seifert, A., Bachmann, V., Filipitsch, F., Förstner, J., Grams, C. M., Hoshyaripour, G. A., Quinting, J., Rohde, A., Vogel, H., Wagner, A., and Vogel, B.: Aerosol–cloud–radiation interaction during Saharan dust episodes: the dusty cirrus puzzle, Atmospheric Chemistry and Physics, 23, 6409–6430, 2023.

Sourdeval, O., Gryspeerdt, E., Krämer, M., Goren, T., Delanoë, J., Afchine, A., Hemmer, F., and Quaas, J.: Ice crystal number concentration estimates from lidar–radar satellite remote sensing – Part 1: Method and evaluation, Atmospheric Chemistry and Physics, 18, 14 327–14 350, https://doi.org/10.5194/acp-18-14327-2018, 2018.

Spichtinger, P.: Shallow cirrus convection – a source for ice supersaturation, Tellus B: Chemical and Physical Meteorology, https://doi.org/10.3402/tellusa.v66.19937, 2014.

Sprenger, M. and Wernli, H.: The LAGRANTO Lagrangian analysis tool – version 2.0, Geoscientific Model Development, 8, 2569–2586, https://doi.org/10.5194/gmd-8-2569-2015, 2015.

Stevens, B., Moeng, C.-H., and Sullivan, P. P.: Large-Eddy Simulations of Radiatively Driven Convection: Sensitivities to the Representation of Small Scales, Journal of the Atmospheric Sciences, 56, 3963 – 3984, https://doi.org/https://doi.org/10.1175/1520-0469(1999)056<3963:LESORD>2.0.CO;2, 1999.

Stevens, B., Moeng, C.-H., Ackerman, A. S., Bretherton, C. S., Chlond, A., de Roode, S., Edwards, J., Golaz, J.-C., Jiang, H., Khairoutdinov, M., Kirkpatrick, M. P., Lewellen, D. C., Lock, A., Müller, F., Stevens, D. E., Whelan, E., and Zhu, P.: Evaluation of Large-Eddy Simulations via Observations of Nocturnal Marine Stratocumulus, Monthly Weather Review, 133, 1443 – 1462, https://doi.org/https://doi.org/10.1175/MWR2930.1, 2005.

Storelvmo, T., Boos, W. R., and Herger, N.: Cirrus cloud seeding: a climate engineering mechanism with reduced side effects?, Philosophical Transactions of the Royal Society A: Mathematical, Physical and Engineering Sciences, 372, 20140 116, https://doi.org/10.1098/rsta.2014.0116, 2014.

Sölch, I. and Kärcher, B.: A large-eddy model for cirrus clouds with explicit aerosol and ice microphysics and Lagrangian ice particle tracking, Quarterly Journal of the Royal Meteorological Society, 136, 2074–2093, https://doi.org/https://doi.org/10.1002/qj.689, 2010.

Tonttila, J., Maalick, Z., Raatikainen, T., Kokkola, H., Kühn, T., and Romakkaniemi, S.: UCLALES–SALSA v1.0: a large-eddy model with interactive sectional microphysics for aerosol, clouds and precipitation, Geoscientific Model Development, 10, 169–188, https://doi.org/10.5194/gmd-10-169-2017, 2017.

Tukiainen, S., O'Connor, E., and Korpinen, A.: CloudnetPy: A Python package for processing cloud remote sensing data, Journal of Open Source Software, 5, 2123, https://doi.org/10.21105/joss.02123, 2020.

Ullrich, R., Hoose, C., Möhler, O., Niemand, M., Wagner, R., Höhler, K., Hiranuma, N., Saathoff, H., and Leisner, T.: A New Ice Nucleation Active Site Parameterization for Desert Dust and Soot, Journal of the Atmospheric Sciences, 74, 699 – 717, https://doi.org/10.1175/JAS-D-16-0074.1, 2017.

Ullrich, R., Hoose, C., Cziczo, D. J., Froyd, K. D., Schwarz, J. P., Perring, A. E., Bui, T. V., Schmitt, C. G., Vogel, B., Rieger, D., Leisner, T., and Möhler, O.: Comparison of Modeled and Measured Ice Nucleating Particle Composition in a Cirrus Cloud, Journal of the Atmospheric Sciences, 76, 1015 – 1029, https://doi.org/https://doi.org/10.1175/JAS-D-18-0034.1, 2019.

Vali, G., DeMott, P. J., Möhler, O., and Whale, T. F.: Technical Note: A proposal for ice nucleation terminology, Atmospheric Chemistry and Physics, 15, 10 263–10 270, https://doi.org/10.5194/acp-15-10263-2015, 2015.

Voigt, C., Schumann, U., Minikin, A., Abdelmonem, A., Afchine, A., Borrmann, S., Boettcher, M., Buchholz, B., Bugliaro, L., Costa, A., Curtius, J., Dollner, M., Dörnbrack, A., Dreiling, V., Ebert, V., Ehrlich, A., Fix, A., Forster, L., Frank, F., Fütterer,

https://doi.org/10.5194/egusphere-2026-2427
Preprint. Discussion started: 12 May 2026

D., Giez, A., Graf, K., Grooß, J.-U., Groß, S., Heimerl, K., Heinold, B., Hüneke, T., Järvinen, E., Jurkat, T., Kaufmann, S., Kenntner, M., Klingebiel, M., Klimach, T., Kohl, R., Krämer, M., Krisna, T. C., Luebke, A., Mayer, B., Mertes, S., Molleker, S., Petzold, A., Pfeilsticker, K., Port, M., Rapp, M., Reutter, P., Rolf, C., Rose, D., Sauer, D., Schäfler, A., Schlage, R., Schnaiter, M., Schneider, J., Spelten, N., Spichtinger, P., Stock, P., Walser, A., Weigel, R., Weinzierl, B., Wendisch, M., Werner, F., Wernli, H., Wirth, M., Zahn, A., Ziereis, H., and Zöger, M.: ML-CIRRUS: The Airborne Experiment on Natural Cirrus and Contrail Cirrus with the High-Altitude Long-Range Research Aircraft HALO, Bulletin of the American Meteorological Society, 98, 271 – 288, https://doi.org/https://doi.org/10.1175/BAMS-D-15-00213.1, 2017.

Weger, M., Heinold, B., Engler, C., Schumann, U., Seifert, A., Fößig, R., Voigt, C., Baars, H., Blahak, U., Borrmann, S., Hoose, C., Kaufmann, S., Krämer, M., Seifert, P., Senf, F., Schneider, J., and Tegen, I.: The impact of mineral dust on cloud formation during the Saharan dust event in April 2014 over Europe, Atmospheric Chemistry and Physics, 18, 17 545–17 572, https://doi.org/10.5194/acp-18-17545-2018, 2018.

Welti, A., Lüönd, F., Stetzer, O., and Lohmann, U.: Influence of particle size on the ice nucleating ability of mineral dusts, Atmospheric Chemistry and Physics, 9, 6705–6715, https://doi.org/10.5194/acp-9-6705-2009, 2009.

Welti, A., Kanji, Z. A., Lüönd, F., Stetzer, O., and Lohmann, U.: Exploring the Mechanisms of Ice Nucleation on Kaolinite: From Deposition Nucleation to Condensation Freezing, Journal of the Atmospheric Sciences, 71, 16 – 36, https://doi.org/10.1175/JAS-D-12-0252.1, 2014.

Zeng, Y., Wang, M., Zhao, C., Zhu, Y., Rosenfeld, D., and Huang, K.-E.: Extremely High Concentrations of Ice Particles in East Asian Dust-Infused Baroclinic Storm (DIBS) Cirrus Shield: Dominant Role of Dust Ice Nucleation Effect, Journal of Geophysical Research: Atmospheres, 128, e2022JD038 034, https://doi.org/https://doi.org/10.1029/2022JD038034, e2022JD038034 2022JD038034, 2023.